Icarus 299 (2018) 411–429

Contents lists available at ScienceDirect

Icarus

journal homepage: www.elsevier.com/locate/icarus

The Ceres gravity field, spin pole, rotation period and orbit from the Dawn radiometric tracking and optical data

A.S. Konopliv[a,*], R.S. Park[a], A.T. Vaughan[a], B.G. Bills[a], S.W. Asmar[a], A.I. Ermakov[a,b], N. Rambaux[c,d], C.A. Raymond[a], J.C. Castillo-Rogez[a], C.T. Russell[e], D.E. Smith[b], M.T. Zuber[b]

[a] Jet Propulsion Laboratory, California Institute of Technology, Pasadena, CA 91109, USA
[b] Massachusetts Institute of Technology, Cambridge, MA 02139–4307, USA
[c] Université Pierre et Marie Curie, UPMC - Paris 06, France
[d] IMCCE, Observatoire de Paris, CNRS UMR 8028, 77 Avenue Denfert-Rochereau, 75014 Paris, France
[e] Institute of Geophysics and Planetary Physics, University of California, Los Angeles, CA 90095–1567, USA

ARTICLE INFO

Article history:
Received 1 May 2017
Revised 26 July 2017
Accepted 2 August 2017
Available online 12 August 2017

ABSTRACT

Ceres' gravity field and rotational parameters have been precisely measured using 1.5 years of radiometric Doppler and range data and optical landmark tracking from the Dawn spacecraft in orbit about the dwarf planet. As was the case with Dawn at Vesta, the gravity field, orientation parameters, landmark locations, and Ceres' orbit are jointly estimated in a global solution. Even though Dawn's radio science investigation at Ceres was complicated by additional thrusting for attitude control, the resulting spherical harmonic gravity field has a half-wavelength resolution of up to 82 km (degree 18) near the equator, which is similar harmonic resolution to that of Vesta. The gravity field is consistent with Airy isostatic compensation, and this model assumption limits Ceres' crustal density to be between 1200 and 1600 kg/m^3 for two-layer and three-layer models with mean crustal thickness between 27 and 43 km. The compensation depth is determined using admittance between gravity and gravity from topography and is superior to admittance between gravity and topography. The gravitational mass of Ceres is determined to better than 0.002% ($GM_{Ceres} = 62.62736 \pm 0.00040$ km^3/s^2), the spin pole location is improved by 10× over previous results with right ascension ($\alpha = 291.427°$) and declination ($\delta = 66.760°$) uncertainty less than 0.001°, and the rotation rate is improved by ~100× over previous determinations from Hubble Space Telescope (HST) images. Ceres' heliocentric orbit has also been improved, with about 17 months of precision range measurements reducing ephemeris uncertainties to about 10 m during the Dawn timeframe.

1. Introduction

The Dawn mission has investigated the two largest objects in the asteroid belt, the proto-planets 4 Vesta and 1 Ceres, with the latter additionally classified as a dwarf planet. The interior of these objects can be studied using the shape derived from the spacecraft image data together with the gravity field, the latter of which is determined from X-band Doppler tracking of the Dawn spacecraft from Earth. The analysis of one-year of Vesta data (Konopliv et al., 2014; Park et al., 2014) shows that the shape and gravity have significant variations from an ellipsoid ($\bar{C}_{22}$, $\bar{S}_{22} > 10\%$ of $\bar{J}_2$) indicating that Vesta is not in hydrostatic equilibrium. The shape and gravity of Ceres, however, is dominated by an ellipsoid of revolution (to about ~3% for gravity and ~5% for shape) showing that this dwarf planet is close to hydrostatic equilibrium (Park et al., 2016). Using the assumption of hydrostatic equilibrium along with the Radau-Darwin relation, the J_2 gravity coefficient, and ellipsoidal shape and spin rate, then the normalized polar ($\bar{C} = 0.39 \pm 0.01$) and mean moments of inertia ($\bar{I} = 0.37 \pm 0.01$) can be determined (Park et al., 2016), where estimates are based upon a volumetric radius of $R = 470$ km and the uncertainties are given by the size of the nonhydrostatic components (Ermakov et al., 2017).

The determination of Ceres' moment of inertia is the major distinguishing characteristic between the gravity investigations of Vesta and Ceres. Without hydrostatic equilibrium, the moment of inertia can only be determined remotely through the measurement of the spin pole precession and nutation together with the J_2 gravity coefficient. For Vesta, the precession and nutation were partly detected, but not well enough to accurately derive the moment of inertia (Konopliv et al., 2014). The benefit of the moments of inertia measurement is to constrain the radial distribution of mass

* Corresponding author.
E-mail address: alex.konopliv@jpl.nasa.gov (A.S. Konopliv).

http://dx.doi.org/10.1016/j.icarus.2017.08.005
0019-1035/

Table 1
Phases of the Dawn mission at Ceres to the conclusion of the lowest altitude LAMO phase and tracking and optical data processed for each phase. The number of observations given for the optical data represents the number of landmark observation pairs (sample,line). The typical number of landmarks in each image is given by the total observations divided by the number of images for that phase.

	Approach + Capture Orbit	Survey	HAMO	LAMO
Begin Time	Feb. 2, 2015 07:53	June 3, 2015 14:50	Aug. 13, 2015 20:34	Dec. 13, 2015 11:52
End Time	May 30, 2015 02:03	July 1, 2015 05:33	Oct. 23, 2015 22:31	Sept. 02, 2016 00:00
Duration (days)	116.8	27.6	71.1	264.2
Number of data arcs	2	2	4	38
Number of Doppler data	30,807	17,009	65,260	246,499
Number of range data	5514	2345	6314	17,770
Number of images/obs.	228 5375	520 25,818	2361 76,899	13,247 41,045
Altitude (km, 470 km sphere)	3946–176,000	4384–4399	1463–1480	366–388
Orbit Period	>3.11 days	3.11 days	18.83 h	5.37 h

within the interior. A completely uniform density sphere has a normalized polar and mean moment of $\bar{C}=\bar{I}=0.4$, whereas a uniform ellipsoid with Ceres' shape has a mean moment of $\bar{I}=0.4$ and polar moment of $\bar{C}=0.420$, when normalized with a mean radius $R_{mean}=\sqrt{(a^2+b^2+c^2)/3}=470$ km. Any concentration of mass toward the center of the body will reduce the normalized moment. For example, the Earth ($\bar{I}=0.33$, Yoder, 1995) shows a greater core concentration than the Moon ($\bar{I}=0.393$, Williams et al., 2014). Other icy bodies include Ganymede ($\bar{C}=0.31$) which is more differentiated, and Callisto ($\bar{C}=0.36$) which may be partially differentiated (Schubert et al., 2004). These mean moments are determined with the assumption of hydrostatic equilibrium where the gravity coefficient J_2/C_{22} ratio is constrained to be 10/3. Since these Galilean satellites are nearly spherical and the mean moment has a similar value, they can be compared to Ceres' mean moment $\bar{I}=0.37$, indicating that it is partially differentiated (Park et al., 2016).

Measurements from the Dawn spacecraft have determined the gravity fields of Vesta and Ceres to similar spherical harmonic resolution. However, there is a striking contrast in the results. The gravity field of Vesta is mostly derived from surface topography assuming a nearly constant density, resulting in a better than a 99% correlation with gravity modeled from a uniform density topography. In contrast, the magnitude of Ceres' gravity field is significantly less and is not represented solely by surface topography. Gravity amplitudes are reduced due to lower crustal density and through a combination of interior structural states such as Airy isostatic compensation (Park et al., 2016; Ermakov et al., 2017; Fu et al., 2017). Compensation occurs where loads on the surface are supported through displacement of a denser interior layer, i.e., buoyancy.

The Dawn spacecraft inserted into orbit about Ceres on March 6, 2015, beginning its multi-year investigation of the dwarf planet. The tracking data processed for this study includes data prior to orbit capture from February 2, 2015 to the conclusion of the Dawn spacecraft in low-altitude orbit about Ceres on September 2, 2016. The higher-altitude data from the Dawn extended mission is not processed for this study. However, it would not substantially improve the gravity investigation results. As with Vesta, the phases of the mission are divided into the following: Approach to Ceres, Survey Orbit, High-Altitude Mapping Orbit (HAMO), Low-Altitude Mapping Orbit (LAMO), with mission dates and number of observations for each phase listed in Table 1. Previous results (Park et al., 2016) show the long-wavelength results of the gravity field to spherical harmonic degree 5 from the Dawn HAMO orbit, whereas here the higher-resolution gravity field from the additional LAMO tracking data is presented to spherical harmonic degree 18.

In similar fashion to the gravity investigation at Vesta (Konopliv et al., 2014), the gravity field and mass of Ceres, the orbit of Ceres around the Sun, the orientation and spin of Ceres, the location of the optical landmarks on the surface of Ceres, and orbits of Dawn with spacecraft force model parameters are jointly determined in a global estimation procedure similar to previous gravity investigations (e.g., Konopliv et al., 2002 for NEAR at Eros; Konopliv et al., 2016 for Mars). Likewise, the primary objective of the Dawn gravity investigation was to determine the gravity field of Ceres to 300 km half wavelength resolution or spherical harmonic degree 5 (Konopliv et al., 2011a). The actual resolution of the gravity field was determined by the altitude of the LAMO mission phase. During this phase, the entire surface of Ceres was sampled at a spacecraft altitude near 365 km relative to the reference 470 km sphere, so that the spacecraft was ~36 km higher over the surface at the poles due to the lower Ceres polar radius. With the LAMO data, the final resolution of the gravity field is much better than the mission requirement and is near spherical harmonic degree 18, or 82 km, which is better than the degree-10 model from previous simulated results (Konopliv et al., 2011a).

In the following sections, we discuss the spacecraft measurements used to determine the dynamical parameters of Ceres, the spacecraft models and coordinate systems implemented, the estimation procedure, the gravity field of Ceres and isostatic compensation results, the rotation of Ceres, landmark estimates and their comparison to the shape model of Ceres, and the heliocentric orbit of Ceres.

2. Spacecraft measurements

2.1. Earth-based tracking

The primary gravity measurement, Doppler tracking, is obtained nearly continuously from the Dawn spacecraft using Earth-based Deep Space Network (DSN) tracking. The DSN station transmits the right-hand, circularly-polarized X-band link frequency at 7.179 GHz for uplink while the downlink signal, for science and engineering telemetry packets, is centered at 8.435 GHz. The two-way (same transmit and receive stations) and three-way (different receive station) coherent mode for radiometric Doppler tracking measures the spacecraft's velocity in the line-of-sight to Earth to typically ~0.05 mm/s or better at 60-second integration times by measuring the Doppler frequency shift in the received signal (see Fig. 1 for Doppler residuals during the LAMO mission phase). Since the gravity field primarily affects the motion or velocity of the spacecraft in orbit about Ceres, the Doppler data, when differentiated with respect to time to yield units of acceleration, are measurements of the gravity field.

The DSN range data do not contribute significantly to the gravity solution, but are the primary measurements for the improvement of Ceres' orbit about the Sun. The range measurement in the spacecraft-Earth direction is accurate to about one meter, but due to uncertainty in the three-dimensional Dawn orbit, the range to the center of Ceres has an error of about 10 m. To determine the

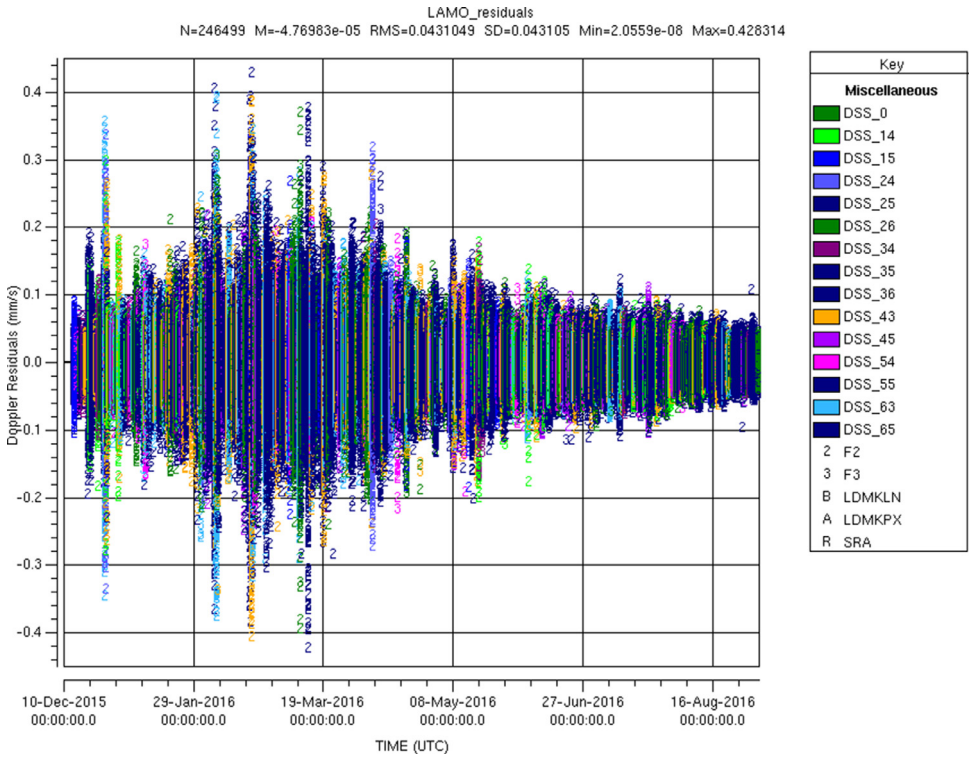

Fig. 1. Dawn 2-way Doppler residuals from the LAMO phase of the mission. The Doppler noise depends on the contribution of solar plasma noise to the X-band link. The noise is greatest for a low Sun-Earth-Ceres angle, which is below 20° for the months of February and March 2016 (see Fig. 2). This angle is a favorable 120° at the end of the LAMO mission phase showing the lowest Doppler noise. The Doppler units are mm/s.

Ceres orbit, we convert the DSN range measurement to the Dawn spacecraft to a range measurement to the Ceres center-of-mass using the Dawn orbit solution around Ceres. As a result, any error in the spacecraft orbit is evident in the range measurement for Ceres.

The Dawn high gain antenna (HGA) is a 1.52-m diameter paraboloid antenna that is fixed to the spacecraft (i.e., does not articulate) to downlink the science and engineering telemetry and has ample signal-to-noise ratio (SNR) margin to achieve the higher Doppler accuracy. However, for much of the mission duration, the HGA is used for only several 8-h tracking passes per week for Doppler and range data, since the spacecraft is nadir-pointed to Ceres to collect science data. Although the spacecraft remains nadir-pointed though much of the mapping mission, and the Dawn high-gain antenna (HGA) is not pointed at Earth, Doppler tracking (but without range data) is obtained though the three available (+X, +Z, −Z) low-gain antennas (LGA) on the spacecraft. The LGAs have just enough link margin with the 34-m DSN stations to collect sufficiently accurate Doppler data, although slightly degraded (∼10%), and with the 70-m DSN antennas, the SNR error contribution is negligible. The vast majority of the Doppler tracking is obtained through the LGAs. Unlike tracking with the HGA, tracking with the LGA antenna induces a signature in the Doppler data due to the motion of the antenna as the spacecraft remains nadir-pointed. This motion is modeled by projecting the LGA antenna location relative to the spacecraft center-of-mass in the Earth direction. The LGA antenna locations are estimated globally using the entire Ceres data set, and the corrections from the nominal positions are on the order of 10 cm.

Media corrections are applied to all Doppler and range data at each DSN complex for daily Earth dry and wet troposphere corrections and daily Earth ionosphere calibrations based upon Global Positioning System (GPS) measurements. Small biases (<0.1 mm/s) are estimated for the 3-way Doppler data to account for station clock errors. The range measurements are corrected for a spacecraft transponder delay and a bias is estimated per DSN pass to account for range calibration errors at the DSN station and is typically less than one meter.

The gravity science data quality depends on several factors such as the effects of media, the angular proximity of the radio beam to the Sun and the received SNR (Asmar et al., 2005). The main consideration for the accuracy of the Doppler is how close the signal passes to the Sun, or the Sun-Earth-Ceres angle. The accuracy of the X-band signal starts to degrade significantly for Sun angles less than 20° (see Fig. 2 of Konopliv et al., 2014); this occurs during the middle of the LAMO mission phase (see Figs. 1 and 2). The Doppler data are weighted differently in the gravity solution as given by the Root-Mean-Square (RMS) of the Doppler residuals for each station pass. As a consequence, data during solar conjunction are included but are de-weighted relative to other Doppler data. Another consideration for the strength of the Doppler data is the geometry of the spacecraft orbit plane as viewed from the Earth and Sun, where typically the gravity field is better determined when viewed edge-on from the Earth as opposed to near face-on geometries. The viewing from both the Sun and Earth show favorable geometry for Dawn (Fig. 2). Although the Doppler accuracy is driven by the above conditions, the actual fit of the data is not necessarily near the Doppler accuracy due to the additional complications of the spacecraft thrusting. Unlike for Dawn at Vesta, where the attitude control was strictly achieved by spacecraft momentum wheels without thrust, the Ceres tracking data is affected by attitude control thrusting about every 5 min.

2.2. Optical landmark tracking

The optical landmark tracking data of Ceres adds considerable strength to the determination of Ceres' spin pole and rotation rate. Additionally, these landmarks constrain the spacecraft orbit to

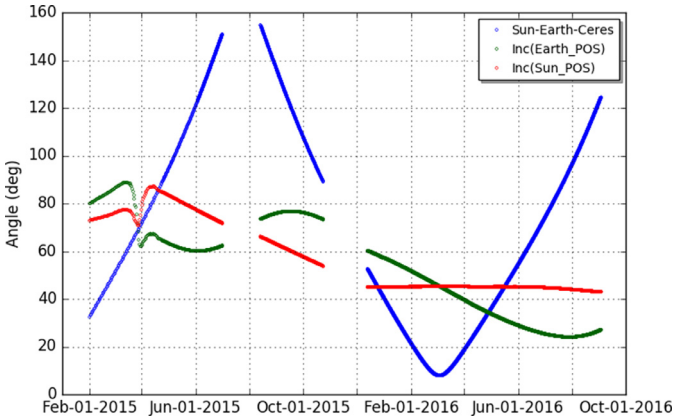

Fig. 2. The Sun angle (Sun-Earth-Ceres, blue), and Plane-of-Sky orbit inclination angles as viewed from the Earth (green) and Sun (red) during the Dawn mission. An inclination angle of 0° indicates the orbit is face-on as viewed from the observer and 90° indicates edge-on. The Sun angle is a minimum (7.9° on March 3, 2016) during solar conjunction. The three mission phases of Survey, HAMO, and LAMO are evident in the plot with gaps in the curves shown for times of the transfer orbits. (For interpretation of the references to color in this figure legend, the reader is referred to the web version of this article.)

Ceres with an accuracy comparable to the pixel size on the surface of Ceres, and collectively these observations greatly improve the orbit uncertainty of the Dawn spacecraft. Indirectly this benefits the estimation of the long-wavelength gravity harmonics, which are correlated with spacecraft orbit. The improved Dawn orbit from landmark tracking also helps the determination of Ceres' heliocentric orbit.

The optical landmark tracking data comes from the Dawn Framing Camera, which collected images of Ceres during all mission phases. The optical observation is the pixel and line location of a landmark in the image. The control vector that defines the landmark is the vector from the center-of-mass of Ceres to the center of a maplet (typically 99×99 pixels). Each maplet also has its own orientation, and every grid point or pixel of the maplet then has a local elevation relative to the frame defined by the control vector and orientation. These local heights are determined in a separate stereophotoclinometry (SPC) process (e.g., Gaskell et al., 2008). Each image (1024×1024 pixels, with a 5.46° field of view) potentially contains many landmarks or maplets. There are over 80,000 landmarks that define the shape of Ceres. Since it requires extensive computational resources to estimate all of the landmark locations in the global gravity solution, we selected a subset of 4004 landmarks to estimate, which are uniformly distributed over the surface of Ceres. The landmark location can be determined in the camera image with an accuracy of about 0.25 pixel after correcting for pointing. This essentially ties the spacecraft's down-track and cross-track position to the Ceres surface with a typical accuracy of 100 m, 35 m and 9 m for the Survey, HAMO and LAMO mission phases, respectively (1 pixel = 93.1 μrad). The typical RMS fit of the optical residuals is about 0.1 pixels (Fig. 3). For both HAMO and LAMO, camera images were processed every 5–20 min during observation campaigns, which resulted in about 300–400 images per week for both phases with an average of 30 and 3 landmarks processed for each image for HAMO and LAMO, respectively. For each image, a camera pointing correction is estimated in both the line and pixel directions with an *a priori* uncertainty of about one pixel (0.005°). The pointing correction is the same for each landmark within the image and the corrections are generally less than one pixel. An additional correction that is estimated for each image is a rotation about the boresight axis or twist and has a smaller *a priori* uncertainty of 0.002° and an estimated correction that is smaller.

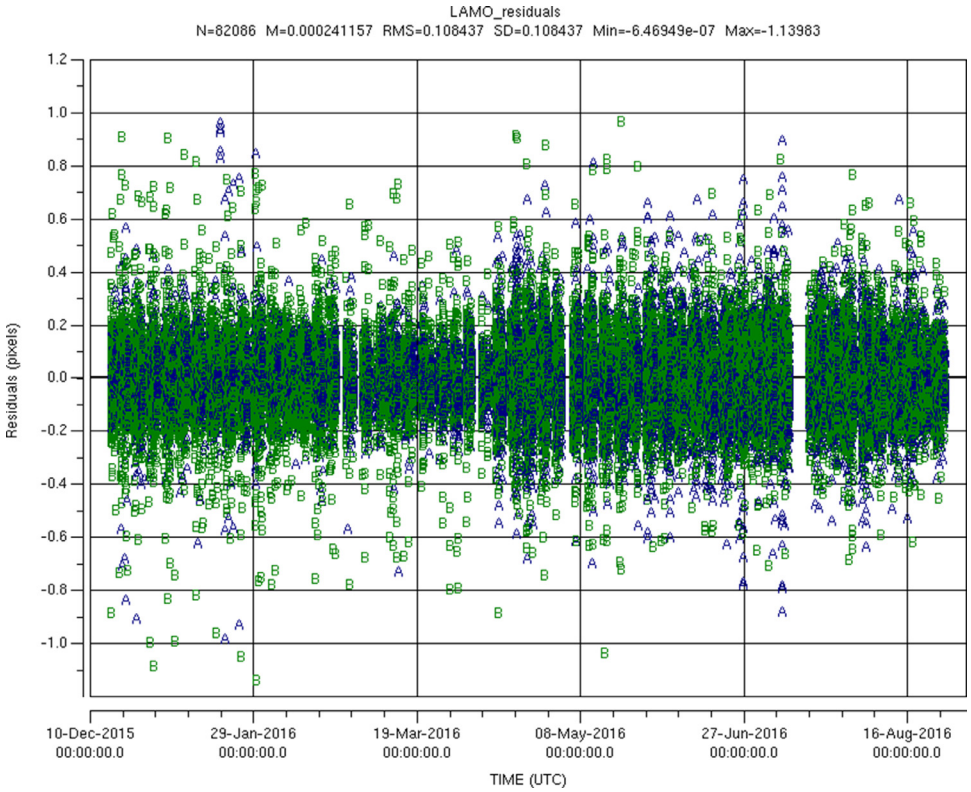

Fig. 3. Optical landmark residuals during the LAMO mission phase. The camera sample direction is blue "A" and the line direction is green "B". The overall RMS of the optical residuals during LAMO is 0.11 pixels. (For interpretation of the references to color in this figure legend, the reader is referred to the web version of this article.)

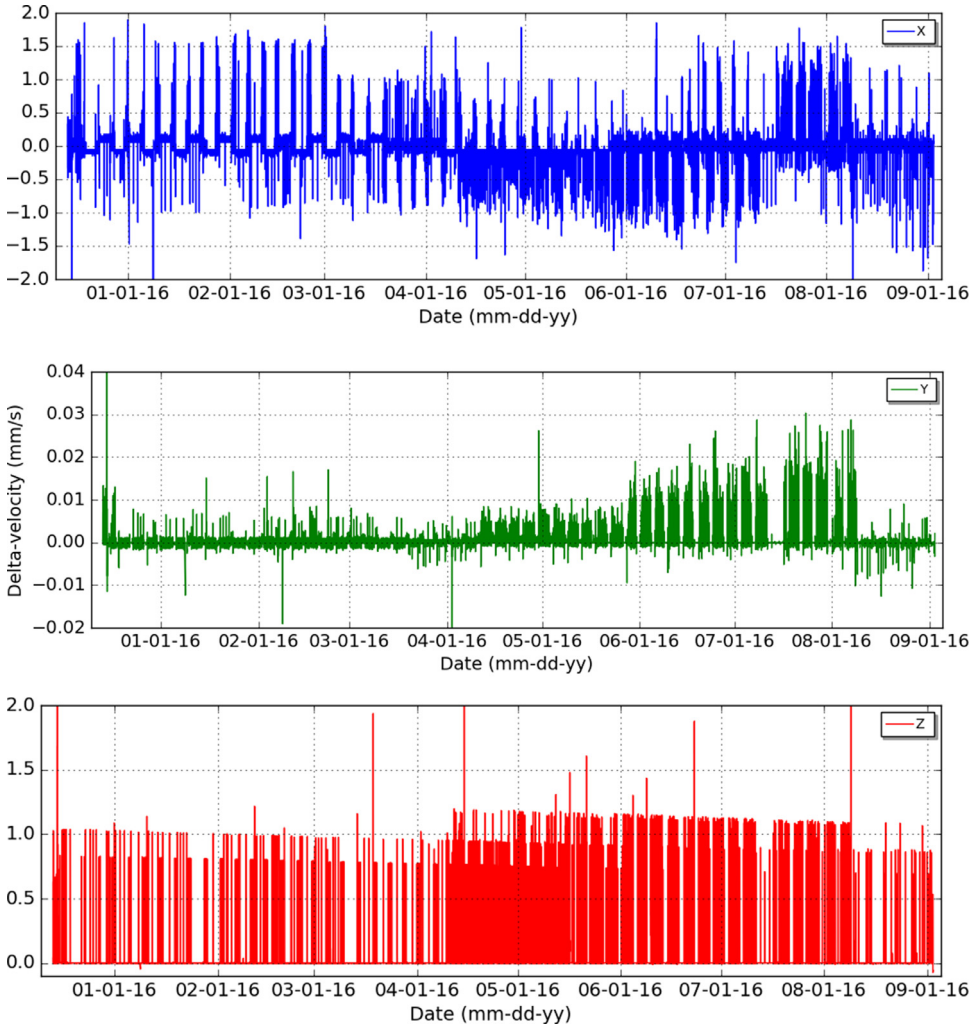

Fig. 4. Attitude maneuvers during the LAMO mission phase in the spacecraft coordinate system directions. There are a total of 145,831 thruster firings during this phase of the mission to maintain the attitude of the spacecraft for hybrid mode, where the two remaining momentum wheels are also used for attitude control. The force in the spacecraft y-direction (along the solar array axis) is noticeably smaller. There are up to three maneuvers in each direction that are off scale. The maximum and minimum maneuver values are x = (1.9,−8.6), y = (0.11,−0.02), z = (6.2,-0.1) mm/s.

3. Spacecraft force models and coordinate frames

Since the Doppler measures the spacecraft velocity, this measurement includes the effect of all forces acting on the spacecraft. To recover the Ceres gravity field and orientation, the effects of the non-conservative forces on the spacecraft must be properly modeled. When the Dawn spacecraft was in orbit about Vesta, the largest force on the spacecraft other than gravity was the solar radiation pressure ($\sim 10^{-11}$ km/s^2). This force is larger ($\sim 4\times$) than the typical solar radiation pressure force on a planetary spacecraft (e.g., Mars orbiters) due to the large solar arrays on Dawn as a result of being a Solar Electric Propulsion (SEP) spacecraft design. Three solar pressure scale factors for each direction are estimated and allowed to adjust within 5% of the *a priori* value. The solar pressure model is a box-wing, flat plate model that represents the spacecraft (Thomas et al., 2011) with three plates for the bus and two plates for the solar array. Pointing of the bus and solar arrays are given by spacecraft telemetry converted to NAIF C-Kernels (Krening, 2012). The solar arrays are Sun-pointed within 2° for the vast majority of the time given by all the arcs processed. In addition, the specular and diffuse reflectivity coefficients of the solar array are estimated globally with the gravity field using the entire Dawn mission tracking and optical data at Ceres.

However, with Dawn at Ceres, the solar pressure is no longer the largest non-gravitational force on the spacecraft. As the Dawn spacecraft departed Vesta in August 2012, a second momentum wheel experienced friction leaving the spacecraft with two momentum wheels for attitude control instead of the required three (the first momentum wheel failed in 2010). As a result, a hybrid mode was established on the spacecraft that used hydrazine thrusters plus the two remaining momentum wheels for attitude control. When in orbit about Ceres, the thrusters fire every few minutes to maintain spacecraft nadir point, with an acceleration imparted to the spacecraft 10–100× greater than the solar pressure force (up to 10^{-9} km/s^2). The history of the thrusting as velocity increments is displayed in Fig. 4; a reconstruction of the small force thrusting by the spacecraft attitude control team using precise thruster on/off times and attitude information. The thrusting is the largest limitation in the recovery of the Ceres gravity field (and the pole location) and the quality of the gravity field and pole solution is dependent on how well this force can be modeled. In comparison to Dawn at Vesta, for example, the uncertainty of Ceres' *GM* (the gravitational constant times the mass of Ceres) is about 40x larger due to the attitude thrusting. The benefit of hybrid mode (e.g., using two momentum wheels) versus no wheels is that the thrusting is reduced and that

the nominal acceleration in the spacecraft y-direction is ~100× smaller.

The attitude thrusting is modeled in three parts. First, a scaling of the reconstructed thrust model from the spacecraft attitude control team is estimated for every data arc. These three factors (one for each spacecraft direction and nominally equal to one) scale the *a priori* model of the spacecraft velocity increments based upon the actual thrust pulses with an *a priori* uncertainty of 10%. Second, a delta velocity correction is estimated for any thrust magnitude greater than 0.2 mm/s accumulated over a time interval of two minutes. The *a priori* uncertainty of the maneuver is 30% of the magnitude expected for each spacecraft direction, but a minimum uncertainty of 0.2 mm/s is used as well. Third, a white noise acceleration is estimated with a batch time interval for LAMO of about 1/4th an orbit (1.35 h) over the duration of the data arc. A batch interval for the other mission phases is about 4 h. The *a priori* magnitude is 5×10^{-11} km/s^2 in the x-direction (along HGA boresight) and z-direction (nadir point during science collection) and again with a smaller 1×10^{-11} km/s^2 acceleration in the y-direction.

The gravitational force on the spacecraft is modeled by a spherical harmonic expansion. The gravitational potential of Ceres in the body-fixed reference frame with normalized coefficients ($\bar{C}_{nm}$, $\bar{S}_{nm}$) is given by (e.g., Heiskanen and Moritz, 1967; Kaula, 1966)

$$U = \frac{GM}{r} + \frac{GM}{r}\sum_{n=1}^{\infty}\sum_{m=0}^{n}\left(\frac{R_e}{r}\right)^n \bar{P}_{nm}(sin\phi_{lat}) \times \left[\bar{C}_{nm}\cos(m\lambda) + \bar{S}_{nm}\sin(m\lambda)\right] \quad (1)$$

where n is the degree, m is the order, $\bar{P}_{nm}$ are the fully normalized associated Legendre polynomials, R_e is the reference radius of the body (470-km for Ceres), ϕ_{lat} is the latitude, and λ is the longitude. The gravity coefficients are normalized such that the integral of the harmonic squared equals the area of a unit sphere, and are related to the unnormalized coefficients as (Kaula, 1966; Lambeck, 1988)

$$\begin{pmatrix} C_{nm} \\ S_{nm} \end{pmatrix} = \left[\frac{(n-m)!(2n+1)(2-\delta_{0m})}{(n+m)!}\right]^{1/2}\begin{pmatrix} \bar{C}_{nm} \\ \bar{S}_{nm} \end{pmatrix}. \quad (2)$$

The degree-one coefficients are zero, since the origin of the coordinate system is chosen to be Ceres' center of mass. The zonal coefficients are given by $\bar{J}_n = -\bar{C}_{n0}$.

The Ceres body-fixed frame is defined by the International Astronomical Union (IAU) coordinate system using right ascension α and declination δ (see Fig. 2 of Archinal et al., 2011) to define the location of Ceres' spin pole in the inertial International Celestial Reference Frame (ICRF). The HST images previously constrained the spin pole location with an uncertainty of about 5° ($\alpha = 291°$, $\delta = 59°$, Thomas et al., 2005). The Dawn mission has reduced the uncertainty by more than a factor of 10^4. The prime meridian W_0 value is chosen to match the Kait crater on Ceres. Prior to Dawn, the best determination of the rotation rate was given by light-curve data (Chamberlain et al., 2007) with $dW/dt = 952.1532 \pm 0.0002$ deg/day. The Dawn optical and Doppler tracking improve the rotation rate by a factor of 100 over the previous results. The orientation model for Ceres does not include the precession of the spin pole, which has a long 227,000-yr period that is over twice the period for Vesta, nor the nutation which has a maximum yearly amplitude of 364 milliarcseconds (Rambaux et al., 2011). These corrections are considered too small to detect.

4. Solution method

The DSN Doppler and range tracking and optical landmark measurements from all Ceres mission phases are processed together to estimate the Ceres gravity field, pole orientation and rotation rate, heliocentric orbit, landmark locations and other spacecraft parameters such as the spacecraft orbit. These observations are processed and filtered using two independent JPL software sets. The first is MIRAGE (Multiple Interferometric Ranging and GPS Ensemble) software program, which is similar to the JPL Orbit Determination Program or ODP (Moyer, 1971, 2000). The landmarks are processed with the Optical Navigation Program or ONP (e.g., Owen et al., 2001). In addition, results were also generated using the second software set MONTE (Mission Analysis, Operations, and Navigation Toolkit Environment), the current operational navigation software at JPL, which processes both the DSN tracking data and landmark observations.

The Ceres gravity field, rotation, landmark locations and other parameters are estimated using a square root information weighted least-squares filter (or SRIF, see Bierman, 1977; Lawson and Hanson, 1995). As part of the solution procedure, the equations of motion of the Dawn spacecraft and linearized variational equations (Tapley et al., 2004) are integrated using a variable order Adams method described in Krogh (1973) that adjusts the integration step size to satisfy specified integration tolerances for each parameter being estimated. The equations are integrated in the ICRF, which is nearly equivalent to the Earth's mean equator at the epoch of J2000 (within < 100 mas, Folkner et al., 1994).

The DSN Doppler and range and optical landmark observations are then processed and the linearized observation equations are formed. Following the nomenclature of Tapley et al. (2004), the observation residual y is given by the difference of the actual observable Y and computed observable using the nominal orbit $Y^*(t)$as given by

$$y = Y - Y^*(t). \quad (3)$$

Using the integrated state transition matrix $\Phi(t, t_0)$to map to the epoch time, the linearized observation equation is then written as

$$y = \left(\frac{\partial G}{\partial X}\right)^* \Phi(t, t_0)x_0 + \varepsilon = Hx_0 + \varepsilon, \quad (4)$$

where X are the parameters being estimated and $Y^* = G(X^*)$ is the equation for the observations. The observation error ε is then minimized using the vector of residuals y and partials matrix H to determine the corrections x_0 to the nominal epoch values of the estimated parameters. In normal form, the least-squares solution $\hat{x}$ is given by

$$\hat{x} = \left(H^T W H + P_{ap}^{-1}\right)^{-1} H^T W y, \quad (5)$$

where W is the weight matrix for the observations and P_{ap} is the *a priori* covariance matrix of the parameters being estimated. In the MIRAGE SRIF filter, the solution equation is kept in upper triangular form

$$R\hat{x} = z \quad (6)$$

when processing observations with Householder transformations and R is the upper triangular square-root of the information array or SRIF matrix, and z is the right-hand side column vector. To improve computational performance since many parameters are estimated (> 10,000 due to landmark position parameters), the filter is parallelized based upon QR factorization (Q is an orthogonal matrix and R is the SRIF matrix) using the publicly available ScaLAPACK software package that is implemented using MPI (Message Passing Interface; see http://www.netlib.org/scalapack).

The DSN tracking data together with the optical data are divided into separate time spans or data arcs for processing. The parameters that are estimated consist of arc-dependent variables (spacecraft position, spacecraft pointing corrections, etc.) that are separately determined for each of the 46 data arcs (see Table 1)

and global variables (e.g., gravity coefficients and landmark positions, with a total of more than 12,000 parameters) that are common to all data arcs. Only the global portions of the SRIF matrices from all the arcs of the entire mission are merged, but this is equivalent to solving for the global parameters plus arc-dependent parameters of all the arcs. Kaula (1966) outlines the technique for partitioned normal matrices. For the Dawn mission at Vesta, the arc lengths were chosen to be as long as possible between orbit maneuvers. However, with the nearly continuous thrusting for attitude control, the arc lengths are typically chosen to be about 7 days long for LAMO and 14 days long for HAMO. There are multiple SEP burns during the LAMO phase (in the months of January, April and June 2016), but all LAMO data arcs are divided such that there are not any SEP burns during the arc. This avoids any contamination of the gravity results by any mis-modeling of the SEP thrusting. The HAMO and Survey arcs also avoid any SEP thrusting.

In summary of previous discussion, the local parameters that are estimated for every arc are spacecraft position and velocity, solar pressure scale factors in three directions, scale factors on the *a priori* burn magnitudes of the attitude thrusting, small velocity increments in all three spacecraft axes directions at the center of the time duration of larger attitude thrusting (>0.2 mm/s), stochastic white noise acceleration, small biases on any three-way Doppler passes (<0.1 mm/s), ranges biases per DSN range pass (1–2 m), and stochastic white noise pointing for the optical data. The global parameters estimated are a 18th degree and order spherical harmonic gravitational potential model and corresponding GM, the initial position and velocity for the ephemeris of Ceres expressed as set III elements which are combinations of classical orbital elements (Brouwer and Clemence, 1961), the Cartesian position locations of the 4000 landmarks, the spin pole right ascension and declination and their rates and rotation rate, the specular and diffuse coefficients of the solar arrays, and the LGA antenna locations.

5. Gravity results for Ceres

The initial Ceres gravity model was determined from the higher-altitude part of the mission (HAMO) and was determined to spherical harmonic degree 5 (spatial block size = 295 km; Ceres08a, Park et al., 2016). With the lower-altitude during the LAMO mission phase, the sensitivity to the gravity field increases, and the Ceres gravity field is estimated to spherical harmonic degree 18 (spatial block size = 82 km). The RMS power spectrum of the new solution from this paper (Ceres18c) is displayed in Fig. 5 and generally follows a $0.0013/n^2$ power law (see Fig. 6). When compared to the error spectrum, the gravity field is determined to about degree 16 (where the signal is greater than the noise), but with additional gravity content up to degree 18, especially for the equatorial regions. The Ceres18c gravity field was determined with a loose constraint on the coefficients, where the coefficient is biased toward zero with an *a priori* uncertainty as is typically done with power law constraints. The *a priori* coefficient uncertainties are 2–10× larger than the RMS amplitudes except for the last two harmonic degrees which are 1.2× larger. The constraint does not significantly change the gravity solution for all but the last two degrees since the $n \leq 16$ harmonics are well determined, in fact coefficient changes are less than 0.1% if the constraint is only applied for $n \geq 14$. It should also be noted that we do not constrain the gravity field to be hydrostatic, as is often done for tidally locked bodies where the ratio of J_2 and C_{22} is 10/3.

In contrast to the results at Vesta, the gravity amplitudes at Ceres are noticeably reduced when compared to the gravity derived from the Ceres shape model (Park et al., 2017) assuming a uniform density of 2162 kg/m^3. This indicates that processes are at work that reduce the topographic load on the surface. Most notably, Airy isostatic compensation of surface topography (Park et al., 2016; Ermakov et al., 2017; Fu et al., 2017) is evident, where the topographic highs can be supported by displacement of a denser interior (i.e., buoyancy). In addition to the observed gravity Ceres18c, Fig. 5 also shows the gravity derived only from the surface topography (i.e., no compensation) assuming a crustal density of 1400 kg/m^3. At the higher degrees ($n > 14$), the amplitude from this crustal model matches the observed gravity. The Bouguer

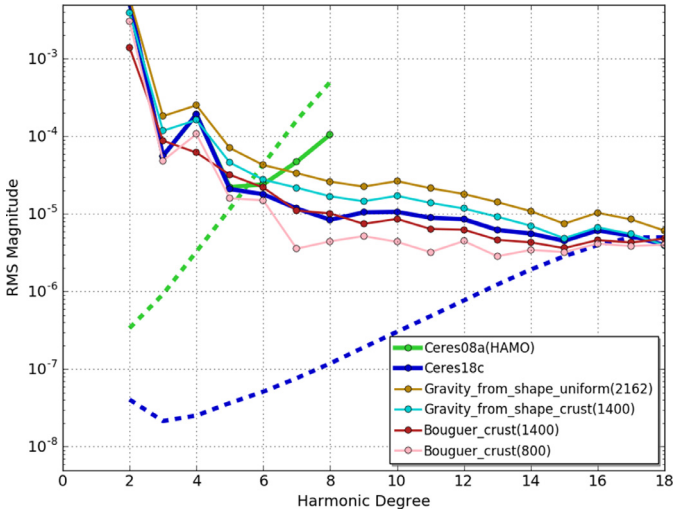

Fig. 5. The Ceres gravity field RMS magnitude spectrum of the spherical harmonic coefficients. The improvement in the gravity field is evident from the HAMO mission phase (Ceres08a; Park et al., 2016) to the LAMO mission phase (Ceres18c), with uncertainties given by the dashed lines. The gravity amplitudes (blue) are noticeably reduced when compared to gravity derived from shape (gold) assuming uniform density equal to the mean density of Ceres (2162 kg/m^3) and for a two-layer model with a spherical inner layer and with crustal density suggested by isostatic compensation models (~1400 kg/m^3, cyan). The two-layer shape models are used to display the difference with the gravity (or Bouguer spectrum) showing the reduced amplitude for degrees $n > 8$ (crustal density 1400 kg/m^3) or $n > 5$ (800 kg/m^3). (For interpretation of the references to color in this figure legend, the reader is referred to the web version of this article.)

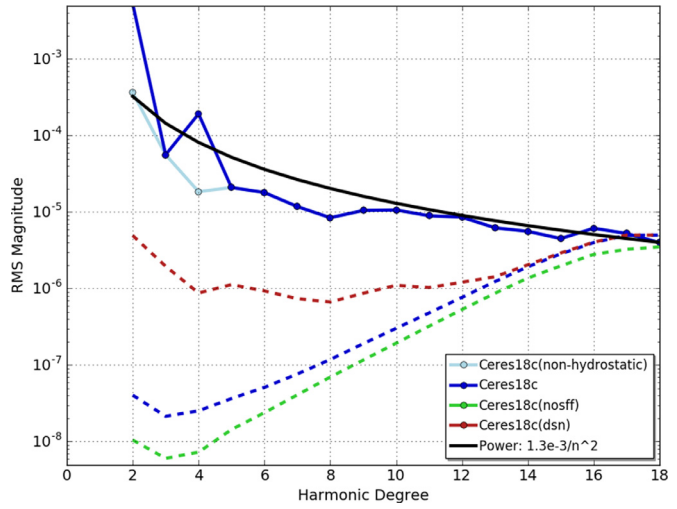

Fig. 6. The Ceres gravity field error spectra from two different cases. The first (nosff) assumes that there were no attitude control maneuvers (i.e., all attitude momentum wheels worked properly) and the second (dsn) assumes there was no optical landmark tracking. The lost momentum wheel on Dawn did not affect the resolution of the gravity field significantly, but only the accuracy of the low-degree harmonics, *GM* and rotational pole. The uncertainty for the DSN only solution shows the very significant contribution of the optical landmark data especially for the low (100×) harmonic coefficient solutions. Two additional curves are shown for informative purposes: the non-hydrostatic spectrum showing the removed J_2 and J_4 coefficients, and the Kaula power law that fits the higher-degree part of the spectrum.

Table 2
Normalized gravity field coefficients of Ceres through degree $n = 8$ for solution Ceres18c (for all degree 18 values see https://sbn.psi.edu/pds/archive/dawn.html). The hydrostatic values for normalized zonal coefficients J_2 and J_4 are also included with an uncertainty given by 6% in shape flattening. Note that for the zonal coefficients $C_{n0} = -J_n$. The corresponding gravitational mass solution is $GM = 62.62736 \pm 0.00040$ km^3/s^2.

Degree n	Order m	C_{nm}	S_{nm}	$\sigma_{C_{nm}}$	$\sigma_{S_{nm}}$
1	0	0	–	0	–
1	1	0	0	0	0
2	0	−1.18508121e-02	–	4.423e-08	–
Hydrostatic value		−1.25789143e-02 ± 0.13e-02	–	–	–
			–	–	–
2	1	4.58448547e-09	3.63916205e-09	2.156e-08	2.154e-08
2	2	2.46972931e-04	−2.74372660e-04	5.213e-08	5.077e-08
3	0	4.15241335e-05	–	1.521e-08	–
3	1	2.33795190e-05	6.21500509e-05	1.948e-08	1.955e-08
3	2	−1.91710411e-05	7.07530736e-05	1.864e-08	1.819e-08
3	3	−4.88336834e-05	−9.00264605e-05	2.877e-08	2.666e-08
4	0	5.72946013e-04	–	2.260e-08	–
Hydrostatic value		5.64715822e-04 ± 1.1e-04	–	–	–
			–	–	–
4	1	−2.27379674e-05	−2.35116082e-06	2.632e-08	2.626e-08
4	2	1.23740596e-05	−1.72200966e-05	2.903e-08	2.915e-08
4	3	−2.34473648e-05	−3.32446852e-06	2.301e-08	2.324e-08
4	4	2.66150658e-05	2.75395714e-05	2.313e-08	2.317e-08
5	0	−3.96953899e-07	–	3.732e-08	–
5	1	1.53188264e-05	−2.22937383e-05	3.702e-08	3.736e-08
5	2	−1.16934614e-05	7.39925646e-06	3.474e-08	3.574e-08
5	3	2.46334954e-05	−2.73340380e-05	4.249e-08	4.239e-08
5	4	−3.33813423e-05	2.20769416e-05	3.165e-08	3.206e-08
5	5	−2.34613423e-05	1.93635198e-05	3.454e-08	3.449e-08
6	0	−2.27582413e-05	–	5.296e-08	–
6	1	6.78874233e-06	2.79510153e-05	5.689e-08	5.767e-08
6	2	−3.50306895e-06	−5.21432009e-06	5.227e-08	5.302e-08
6	3	−9.87277872e-06	3.85202285e-05	5.067e-08	5.057e-08
6	4	1.06754082e-05	−8.36138236e-06	5.158e-08	5.137e-08
6	5	2.25359280e-05	−3.92256270e-06	4.965e-08	4.976e-08
6	6	−2.23049266e-05	−5.80614538e-06	4.274e-08	4.271e-08
7	0	1.55434338e-06	–	8.387e-08	–
7	1	−1.01359374e-06	−6.69691442e-07	8.673e-08	8.737e-08
7	2	2.40321407e-05	−5.90292779e-06	8.088e-08	8.196e-08
7	3	−1.83100389e-05	−6.96434307e-06	7.471e-08	7.443e-08
7	4	1.23357708e-05	−1.07523753e-05	6.797e-08	6.776e-08
7	5	2.66520724e-06	−2.33239302e-05	8.073e-08	8.129e-08
7	6	6.61491836e-07	−4.65656724e-06	7.449e-08	7.421e-08
7	7	5.24659268e-06	−1.44939379e-05	6.116e-08	6.146e-08
8	0	5.81457263e-06	–	1.376e-07	–
8	1	−5.52943496e-06	−1.25700137e-06	1.404e-07	1.410e-07
8	2	−1.58363864e-05	7.01695837e-06	1.339e-07	1.356e-07
8	3	−8.82195279e-06	3.05664113e-07	1.197e-07	1.206e-07
8	4	−3.14244376e-06	1.11675420e-05	1.063e-07	1.065e-07
8	5	3.13819286e-06	4.88561586e-06	1.087e-07	1.085e-07
8	6	1.37076971e-06	−1.40319815e-05	1.156e-07	1.152e-07
8	7	−1.05089714e-05	1.35521571e-05	1.140e-07	1.132e-07
8	8	3.87039879e-06	9.26139704e-06	8.887e-08	8.837e-08

gravity spectra (gravity minus the gravity associated with topography accurately determined by volume integrals) for both 800 and 1400 kg/m^3 crusts are also displayed. We note that Bouguer amplitudes are minimized for a crustal density of 800 kg/m^3 for degrees $n \geq 5$. The 1400 kg/m^3 crustal density in Fig. 5 and used throughout this paper is intermediate between several crustal densities considered in this paper (1200, 1400 and 1600 kg/m^3), which are consistent with isostatic compensation as discussed later. The lowest density evaluated is 1200 kg/m^3, which is near the density that minimizes the Airy isostatic anomalies assuming a two-layer model with the observed moment of inertia (1287 kg/m^3 in Ermakov et al., 2017). However, the Bouguer anomalies for n = 2 and 4 (essentially the hydrostatic component of J_2 and J_4) are minimized for higher densities of 1600–1900 kg/m^3 for a two-layer model.

Although spacecraft attitude thrusting is the major source of error in the gravity field determination, the loss of the Dawn spacecraft momentum wheel did not significantly reduce the resolution of the gravity field compared to what would have been if all momentum wheels were available. Fig. 6 displays the gravity spectrum uncertainty for the case where no attitude control maneuvers or stochastic acceleration were estimated. The largest effect is in the lower degrees of the spectrum and with up to a factor 10 degradation in the *GM* and rotation solution uncertainties. The DSN-only gravity uncertainty curve in Fig. 6 estimates the attitude thrusting as in the nominal case but removes the optical landmark tracking data in the solution. Again, the resolution of the gravity field is not reduced, but the necessity of the optical landmark tracking is clearly evident in the uncertainties of the low and medium harmonics. The optical data probably helped mitigate the degradation due to the attitude control thrusting. However, due to the attitude control thrusting, we adjust the Ceres18c uncertainty by scaling the individual coefficient rows of the SRIF matrix before inversion (Konopliv et al., 2016). Based upon differences between solutions using different data subsets and attitude thrusting assumptions, the low-degree harmonics up to degree 5 are scaled

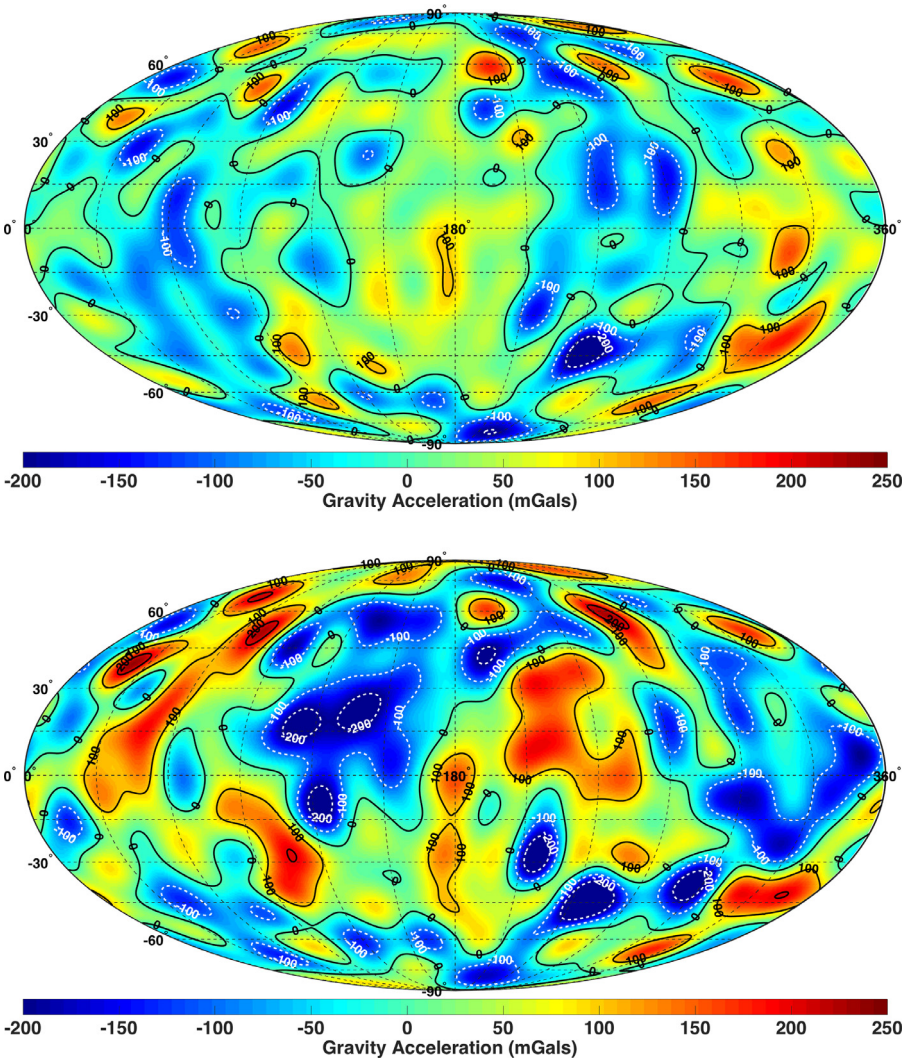

Fig. 7. The observed radial gravity acceleration (top) and modeled radial gravity from a two-layer shape model with crustal density of 1400 kg/m^3 (bottom). Accelerations are mapped to a 482.0 × 445.9-km ellipsoid of revolution for degree $n = 2$–16. The large hydrostatic zonal gravity coefficients J_2 and J_4 are omitted in the accelerations. The maximum and minimum gravity amplitudes are 186 and −282 mGals. The minimum is at the crater Urvara (250°E, 45°S).

by 3x and then other coefficients are scaled linearly to 1x at degree 18. This provides more realistic errors to account for the attitude thrusting and red-noise characteristics of the solar plasma in the Doppler data. Fig. 6 additionally shows the power law ($0.0013/n^2$) that fits the higher-degree part of the spectrum and is substantially less than the power law scaled from the Earth ($0.0086/n^2$, Konopliv et al., 2011).

The Ceres gravity degree 2 and 4 coefficients are dominated by the hydrostatic contribution from J_2 and J_4. The unnormalized hydrostatic zonal values are given by (e.g., Yoder, 1995)

$$J_2 \approx \frac{1}{3}\left(2\tilde{f} - \tilde{m}_v + \frac{11}{49}mf^2\right)$$
$$J_4 \approx -\frac{15}{7}J_2^2 + \frac{5}{21}\left(\frac{4}{5}\tilde{f} - \tilde{m}_v\right)^2 \quad (7)$$

where the flattening $f = \frac{a-c}{a} = 0.074896$, and $a = 482.0$ km is the equatorial radius and $c = 445.9$ km is the polar radius (values from Park et al., 2016), $\tilde{m}_v = m(1-f)(1-\frac{2}{7}f)$, $m = \omega_s^2 a^3/\mathrm{GM}$, $\tilde{f} = f(1-\frac{1}{2}f)$, and ω_s is the spin rate. We also note that the hydrostatic J_4 computed from Yoder (1995) assumes a homogeneous shape, and is a good match for the observed value. An alternate expression for the hydrostatic J_4 is given by Rambaux et al. (2016), where the corresponding formula require the use of the computed hydrostatic a and c values in order to match the observed J_4. If one uses the observed Ceres shape a and c directly, then the computed J_4 is significantly different from the observed value. The low-degree gravity coefficients for Ceres18c are given in Table 2 and include the hydrostatic range of values from the above equations as well. The uncertainties in the hydrostatic gravity values are determined using an uncertainty of 6% in the shape flattening, since a component of the flattening is non-hydrostatic. The flattening error percentage is derived from the ratio of the tesseral coefficients relative to the zonal values for the topography and is about a factor of two greater than the corresponding ratio for the gravity coefficients.

The mass of Ceres was previously determined by its perturbation of the orbit of Mars (e.g. Standish, 2001; Pitjeva, 2005; Konopliv et al., 2006; Konopliv et al., 2011b; Fienga et al., 2009; Kuchynka and Folkner, 2013) and from close flybys with other asteroids (e.g., Michalak, 2000; Baer et al., 2011), with an uncertainty of about 1%. With the Dawn spacecraft in orbit, the mass estimate of Ceres is now known to about 0.002% (see Table 2).

The acceleration of both the observed gravity field Ceres18c and the gravity derived from topography assuming a two-layer model with a constant crustal density of 1400 kg/m^3 and a spherical inner layer are displayed in Fig. 7. The map shows the radial

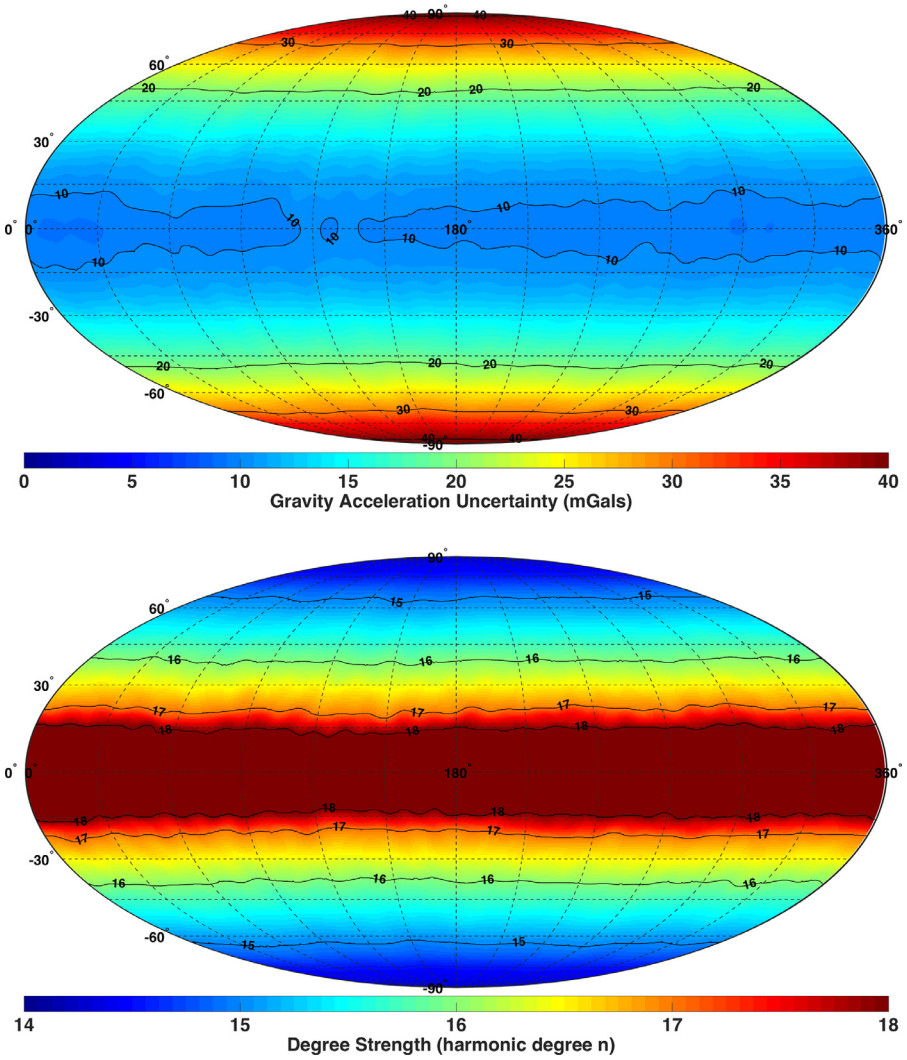

Fig. 8. The gravity uncertainty in the radial acceleration from the full Ceres18c covariance (including hydrostatic terms) on a 482.0 × 445.9-km ellipsoid of revolution for harmonic degrees $n = 2$–16 (top), and the degree strength or resolution on the same ellipsoid (bottom). The degree strength is calculated using the observed RMS spectrum of Ceres to be the power law $0.0013/n^2$.

acceleration near the surface as given by an ellipsoid of revolution with the above flattening ($f = 0.074896$) for the harmonic degrees 2–16, except the larger hydrostatic J_2 and J_4 coefficients are not included. The differences in large-scale areas such as Vendimia Planitia (centered at 140°E and 20°N) and Hanami Planum (230°E and 20°N) (represented in harmonic degrees 2 and 3) are evident, where the gravity from topography displays large areas of negative and positive, respectively, and the observed gravity is significantly smaller.

The radial acceleration uncertainty of the Ceres18c gravity model on the same ellipsoid near the surface is displayed in Fig. 8. The results from mapping the full covariance give uncertainties that are near 10 mGals at the equator and increase to 40 mGals at the pole due to the higher-altitude of the Dawn spacecraft relative to the surface. Fig. 8 also shows the resolution of the Ceres gravity field over the surface by mapping the covariance to the same ellipsoid to obtain the degree strength (Konopliv et al., 1999). This is the harmonic degree where the uncertainty in the acceleration for that degree is equal to the expected amplitude for gravity coefficients of only that degree. The expected amplitude of the gravity acceleration is given by the observed Kaula power law $0.0013/n^2$ (see Fig. 6), which corresponds to a surface acceleration profile of $52/n^{1/2}$ mGals per degree. As a result, the equatorial region is determined to harmonic degree 18 whereas the polar regions are determined to degree 14. When one determines the radial acceleration error on the ellipsoid to only degree 14, the maximum error at the poles reduces from 40 mGals to 12 mGals.

In addition to the errors in the gravity field due to measurement and model accuracies, we also investigated errors due to the convergence of the spherical harmonic gravity field near the surface. The spherical harmonics are known to converge outside the smallest sphere that encloses Ceres (e.g. the Brillouin sphere of ~ 482-km, Grafarend and Engels, 1994; Heiskanen and Moritz, 1967), so convergence anywhere except near the equatorial region is unknown. Ellipsoidal harmonics, however, will converge outside the smallest ellipsoid that encompasses the body and are valid near the entire surface of Ceres. Thus, to check the errors due to spherical harmonic convergence, we also generated an ellipsoidal harmonic gravity model of Ceres and compared the mapping of both to the ellipsoid near the surface (482.0 × 445.9 km). The maximum differences were ~50 mGals near the polar regions (or ~1.25× the covariance uncertainty) for harmonic degrees 2–16, and indicate the convergence errors for the spherical harmonics are small enough to neglect for Ceres.

The half-wavelength resolution of Ceres18c to degree 16 is 11.25° or 92-km for the mean 470-km radius. Multiple craters

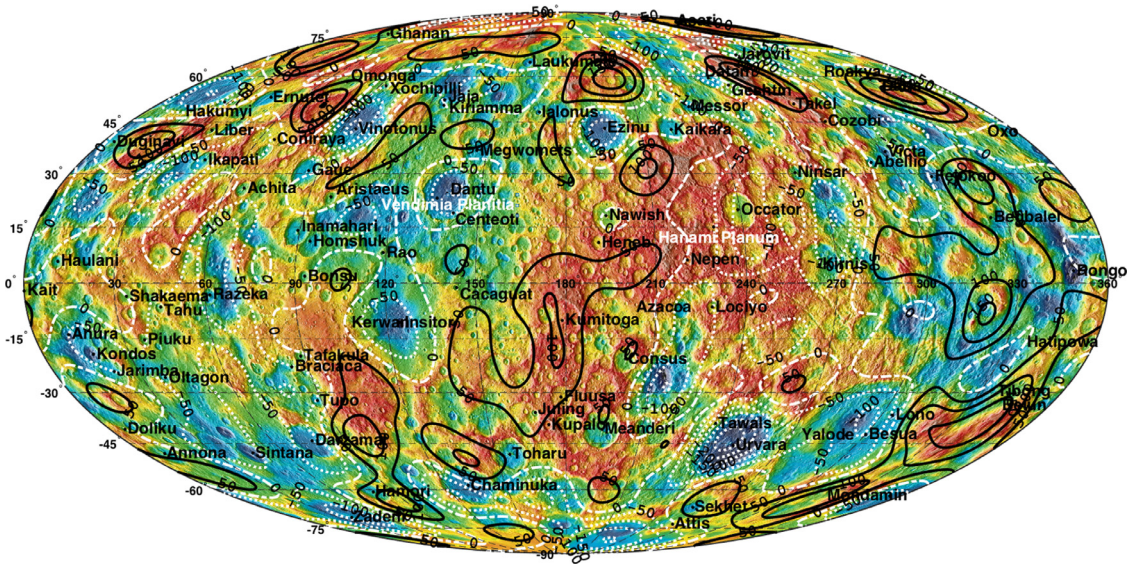

Fig. 9. The Ceres gravity field displayed as contour lines on a topographic surface feature map of Ceres. The gravity field includes coefficients from degree $n=2$ to degree $n=16$ except for the J_2 and J_4 coefficients. Positive (radial inward) gravity contour lines are displayed as solid black and negative gravity contours are dashed white lines. Contour intervals are 50 mGals.

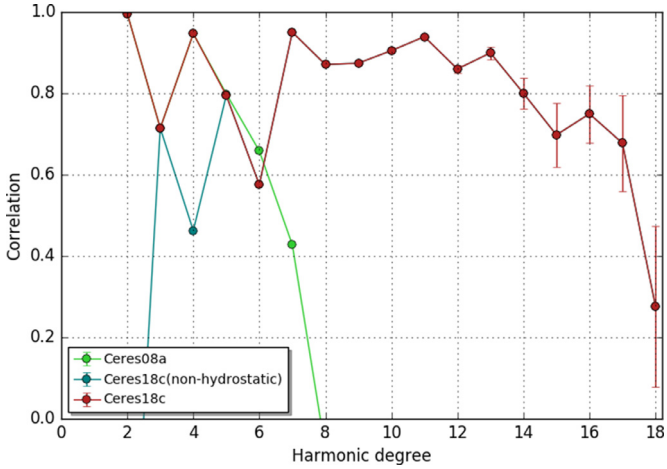

Fig. 10. Correlation of the Ceres gravity field with the gravity derived from the topography assuming constant density (correlations are independent of crustal density). The correlations of the hydrostatic coefficients dominate the degree $n=2$ and 4 correlations. Without J_2 and J_4 in the correlations (i.e., "non-hydrostatic"), the correlations for degree $n=2$ (−0.71) and 4 (0.46) are much smaller. This improvement from the HAMO portion of the mission (Ceres08a: Park et al., 2016) is evident. Correlation errors using the full gravity covariance of Ceres18c are included.

slightly larger than this resolution are resolved in the gravity field. Fig. 9 displays the gravity field to degree 16 as contours over a topographic surface feature map, and the resolution of craters becomes evident. There are circular gravity minima for Vinotonus (95°E, 40°N), Dantu (140°E, 25°N), Ezinu (195°E, 40°N), Zandeni (40°E, 70°S), Urvara (250°E, 45°S), and Mondamin (350°E, 35°S).

The information content of each degree of the gravity field becomes apparent with the correlation of the observed gravity field and the gravity derived from the shape of Ceres (Fig. 10). The low-degree harmonics ($n=2$–6) show long-wavelength and deep interior structure changes (lower correlations). Once the hydrostatic coefficients are removed, the degree $n=2$ correlation for C_{22} and S_{22} is negative (−0.71), and degree $n=4$ is noticeably reduced. For harmonic degrees 6 or greater the correlation is near 0.9 to $n=13$, and thus the gravity field is well determined to this degree. Beginning with $n=14$ and higher, the gravity field is mostly determined to degree 17 since one would expect correlations near 0.9 for those degrees as well. Fig. 10 also displays the uncertainty in the correlation using the full gravity covariance for each harmonic degree and assuming the gravity from topography is perfectly known. With $\mathbf{G}_n$ and $\mathbf{T}_n$ being the vector of all gravity and gravity from topography coefficients (assuming uniform mean density 2162 kg/m^3) for degree n, respectively, the correlation for degree n is given by

$$\gamma_n = (\mathbf{G}_n \bullet \mathbf{T}_n)/(G_n T_n), \tag{8}$$

where G_n and T_n are the magnitudes of the corresponding vectors. The correlation error bars for each degree (σ_{γ_n}) are contributions from the gravity covariance and are given by

$$\sigma^2_{\gamma_n} = \mathbf{A}^T_n \mathbf{P}_n \mathbf{A}_n, \tag{9}$$

where the matrix $\mathbf{P}_n$ is the sub-covariance with only the degree-n terms ($\mathbf{G}_n$) of the full covariance matrix of Ceres18c. The vector $\mathbf{A}_n$ is the partial of the correlation for degree n (γ_n) with respect to the gravity coefficients of degree n,

$$\mathbf{A}_n = (\mathbf{T}_n/G_n T_n) - \gamma_n(\mathbf{G}_n/G^2_n). \tag{10}$$

The errors shown in Fig. 10 indicate that the higher degree ($n>13$) correlations are generally within two standard deviations of the correlation values for the mid-harmonics ($n=7$–13).

As discussed previously, the Ceres gravity model displays significantly reduced amplitudes consistent with Airy isostatic compensation. The most common approach to determine the depth of compensation from the spherical harmonic coefficients is to calculate the admittance Z_n between the topography and gravity coefficients for each degree n, where $Z_n=(\mathbf{G}_n \bullet \mathbf{B}_n)/B_n{}^2$ and $\mathbf{B}_n$ is the vector of topography coefficients of degree n. The admittance is related to the compensation depth D_n of each degree by (Turcotte and McAdoo, 1979)

$$Z_n = \frac{3\rho_{crust}}{(2n+1)\rho_{mean}}\left[1-\left(1-\frac{D_n}{R}\right)^n\right]. \tag{11}$$

In Eq. (11), we assume isostasy with spherical equal mass columns, and this is slightly different from isostasy with equal pressure, where an extra factor g_t/g_b is added (e.g., see Hemingway and Matsuyama, 2017; Ermakov et al., 2017) and g_t is the gravity at the top of the compensated layer and g_b is the gravity at its bottom. In this case the exponent also becomes $n+2$ since

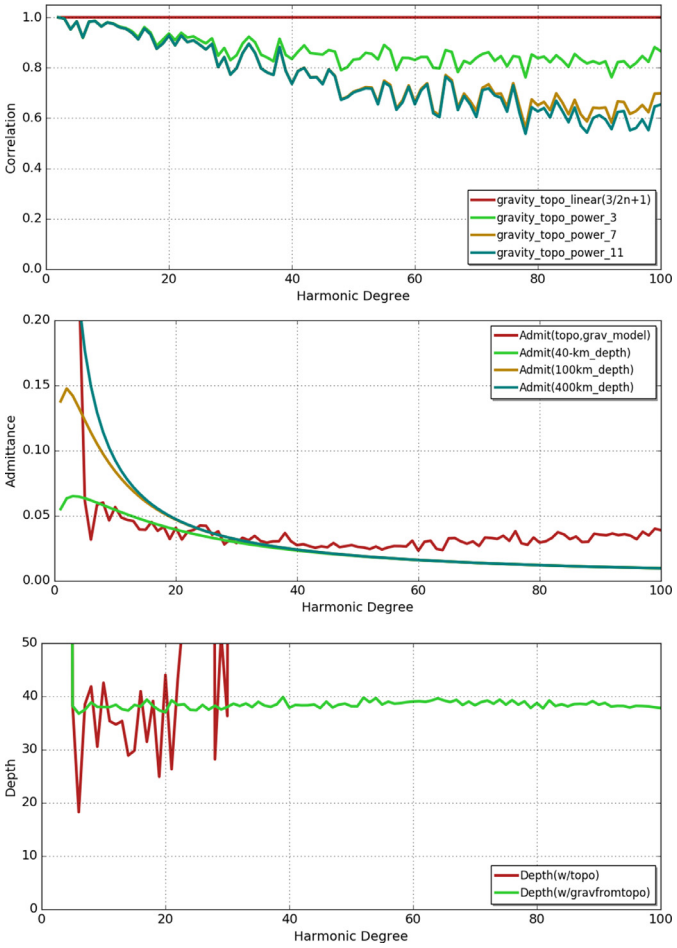

Fig. 11. Simulation results on techniques to recover compensation depth. The correlation (top) of topography with gravity derived from topography for various powers of topography show the significant contributions from the nonspherical shape of Ceres. The admittance (middle) of simulated gravity and topography shows that the typical method of computing compensation depth breaks down for degrees $n > 30$. The admittance at this point is greater than any theoretical admittance for all depths (40-km, 100-km, and 400-km are shown). The recovered depth in km (bottom) show the proposed method of using admittance of gravity from topography and gravity properly recovers the depth whereas the admittance of topography and gravity (red) tends to underestimate the depth when valid. . (For interpretation of the references to color in this figure legend, the reader is referred to the web version of this article.)

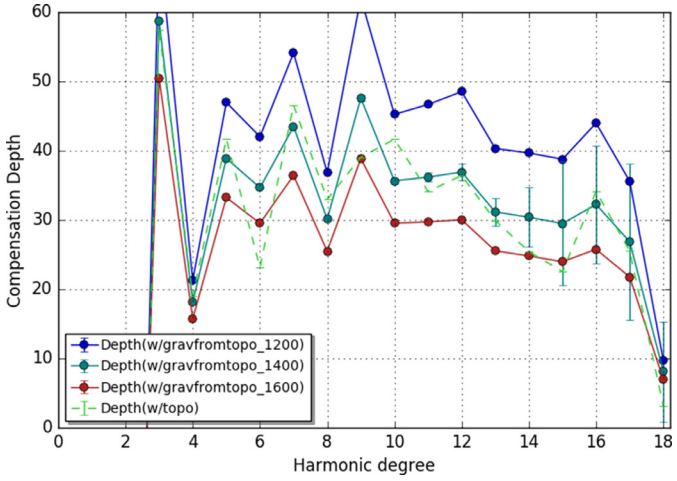

Fig. 12. Airy isostatic compensation depth versus degree assuming constant crustal densities of 1200, 1400 and 1600 kg/m^3. The error bars for density 1400 kg/m^3 show the uncertainty in the depth versus degree due to the gravity field only and assuming the gravity from topography is perfectly known. The gravity errors are derived from a full covariance for all gravity coefficients of a given degree and the depths for degree $n = 2$ and 4 are for the non-hydrostatic coefficients. Also shown is the depth from the admittance from topography and gravity (dashed) for a crustal density of 1400 kg/m^3.

Hemingway and Matsuyama (2017) argue against spherical equal mass. The differences in compensation depths between the models are largest at the lower harmonic degrees. Ermakov et al. (2017) use a different approach to define isostasy. Their approach is based on the viscous relaxation of a two-layer model. Ermakov et al. (2017) provide factors w_n (ratio of crust-mantle depth or root to surface topography height), and corresponding compensation depths increase by ~5 km versus the assumption of equal mass columns for a 40 km compensation depth.

One expects the compensation depth to be the same for all degrees, but calculating per degree shows the possible range of values for depth. The admittance method of Eq. (11) assumes the body is nearly spherical and neglects nonlinear contributions in the conversion between gravity and topography (i.e., gravity from topography is computed to power one of topography). Since Ceres is substantially flattened and has a non-spherical shape, we propose an alternative method for determining the compensation depth by using the admittance $\tilde{Z}_n$ between the gravity derived from topography (again assuming uniform density 2162 kg/m^3) and gravity, $\tilde{Z}_n = (\mathbf{G}_n \cdot \mathbf{T}_n)/T_n^2$. In this case, the depth is related to the admittance by

$$\tilde{Z}_n = \left[1 - \left(1 - \frac{D_n}{R}\right)^n\right]. \quad (12)$$

In order to determine which method is best to estimate the compensation depth, we did a simulation to see how well each recovers a given depth. Using the actual topographic model of Ceres (Park et al., 2017), we developed a truth gravity model using two-layers. The first layer consists of a uniform crust ($\rho = 1400$ kg/m^3) and the second layer is a mantle ($\rho = 2395$ kg/m^3) represented by a Moho (i.e., compositional) boundary with 40-km depth and with spherical Airy compensation assuming spherical equal mass columns beginning at degree 5 (the first degree past the hydrostatic contributions). The mantle density was inferred to meet the mean density of 2162 kg/m^3. All degree 2 to degree 4 spherical harmonic coefficients of the Moho are zero except for J_2 and J_4 so that the ellipsoidal shape of the Moho is the same as the crust with the semi-major axes reduced by 40-km. The gravity of the two layers are then computed to power 11 of topography (Wieczorek and Phillips, 1998), and then combined.

For the simulation, we now have the observed gravity (as given by the truth model with a compensation depth of 40-km) and the observed topography. We apply both admittance equations to see how well we recover the compensation depth. The simulation results are displayed in Fig. 11. As shown in the figure with the correlation between topography and gravity derived from topography to various powers of topography, there are significant nonlinear contributions in the gravity derived from topography. For harmonic coefficients to degree 20, topography to power 3 must be used whereas to degree 100, topography to power 11 is required. The admittance between topography and gravity is also shown in Fig. 11 along with the theoretical admittance for compensation depths of 40-km, 100-km, and 400-km (to see the full range of possible admittance). One can see that the linear technique does not work for coefficients $n > 30$ since there is no compensation depth that satisfies the observed admittance. This is due to the nonlinear contributions from the shape of Ceres. Finally, the recovered compensation depths are shown in Fig. 11 for both cases. The admittance from gravity derived from topography and gravity cor-

Table 3
Model parameters of the Ceres interior for three different crustal densities assuming Airy isostatic compensation. The moments of inertia ($R = 470$ km) are displayed for two-layer models for each case. In order to match the observed mean moment of inertia the higher crustal densities require an interior density concentration or core. In the three-layer case, the density shown is for an assumed concentration of 200-km radius. The observed Ceres moments of inertia are $A = 0.362$, $B = 0.363$, $C = 0.389$, $I_{mean} = 0.371$ (Park et al., 2017).

Parameter	Crustal Density 1200 kg/m^3	Crustal Density 1400 kg/m^3	Crustal Density 1600 kg/m^3
Mean Crustal Thickness or Compensation Depth (km)	43	33	27
2-layer moment of inertia:			
A	0.361	0.373	0.380
B	0.361	0.373	0.380
C	0.390	0.403	0.410
I_{mean}	0.371	0.383	0.390
2-layer mantle density (kg/m^3)	2470	2340	2260
3-layer moment of inertia:	–		
A		0.362	0.362
B		0.362	0.362
C		0.390	0.390
I_{mean}		0.371	0.371
3-layer mantle density (kg/m^3)	–	2225	2090
3-layer core density 200-km core size (kg/m^3)	–	3410	3960

rectly recovers the compensation depth, whereas the admittance of topography and gravity shows much larger scatter and tends to underestimate the compensation depth.

The uncertainties in the compensation depth versus degree can be determined in similar fashion to the correlation errors. Using the gravity derived from topography, the Airy isostatic compensation depth per degree D_n can be solved for and is given by

$$D_n = R - R\left(1 - \tilde{Z}_n\right)^{1/n}, \tag{13}$$

where $\tilde{Z}_n$ is the admittance between the gravity and gravity from shape for reference radius $R = 470$ km. The uncertainty in the compensation depth due to measurement errors in the gravity model alone is then given by

$$\sigma_{D_n} = \frac{R}{nT_n^2}\left(1 - \tilde{Z}_n\right)^{\frac{1}{n}-1}\left(\mathrm{T}_n^T \mathrm{P}_n \mathrm{T}_n\right)^{1/2}. \tag{14}$$

The crustal thickness or isostatic compensation depth for Ceres is only a function of the crustal density, where a thicker crust is required for smaller crustal densities. The compensation depths versus harmonic degree for three different crustal densities (1200, 1400, and 1600 kg/m^3) are displayed in Fig. 12. The maximum crustal thickness in Fig. 12 (~43 km) uses the gravity from shape with a crustal density of 1200 kg/m^3 (similar to 1287 kg/m^3 of Ermakov et al., 2017), and the compensation depths and errors are consistent with other isostatic studies (~40 km, Ermakov et al., 2017). The corresponding crustal thicknesses for 1400 and 1600 kg/m^3 are 33 km and 27 km, respectively. One would expect the compensation depths from the well-determined higher degrees to give a truer indication of the depth, since deeper mass variations are attenuated more at the surface for higher degrees. For this reason, the depth given here is taken as the average from degrees 10 to 16. Although not the preferred method, the depths from admittance from topography are also shown for 1400 kg/m^3 for comparison and generally displays less depth at higher degrees.

Three Airy isostatic compensation interior models for three different crustal densities of 1200, 1400, and 1600 kg/m^3 are presented in Table 3 for both two-layer and three-layer cases. The crustal density of 1200 kg/m^3 (Ermakov et al., 2017) requires only a two-layer model since the model moments of inertia match the observed moments (Park et al., 2017). This model represents the minimum crustal densities that are possible for Airy compensation models. Any crustal density smaller than 1200 kg/m^3 requires a density inversion (i.e., decrease in density with depth) in order to match the observed moment of inertia from hydrostatic equilibrium. For crustal densities greater than 1200 kg/m^3, a concentration of mass in the interior is required in order to match the observed moment of inertia. The core size is assumed to be 200-km, but the models can be adjusted for other assumed core sizes. The crustal density of 1600 kg/m^3 represents the maximum feasible crustal density for compensation models. At this density, the crustal thickness becomes negative for some smaller regions due to the smaller density contrast between the crust and mantle.

The corresponding isostatic anomaly map for crustal density of 1400 kg/m^3 (Fig. 13) shows the difference between gravity and gravity from shape corrected for the average admittance per harmonic degree ($\mathbf{I}_n = \mathbf{G}_n - \tilde{Z}_n \mathbf{T}_n$), i.e., assuming a linear relationship between the gravity and gravity from shape (again modified from the typical gravity and topography admittance). The RMS isostatic differences (~20 mGals) are noticeably smaller by about a factor of two than the corresponding Bouguer map, where the gravity is derived from the surface topography with a uniform density of 1400 kg/m^3. The isostatic anomalies show the difference from the global average compensation of each harmonic degree n at the Moho boundary. If for a positive anomaly, the isostatic anomaly is negative, then the feature has more compensation than the global average. If the gravity and isostatic anomalies are both positive (such as the gravity and topographic high at 195°E, 60°N), then there is less compensation.

Another evaluation of the gravity field is to determine if it is isotropic or if there is a preferred direction with larger gravity anomalies. From Bills and Lemoine (1995), the mean square north-south slope variance $T_n(N\text{-}S)$ and the mean square east-west slope variance $T_n(E\text{-}W)$ for degree n are given by

$$T_n(N-S) = \sum_m N_{nm} G_{nm}^2$$
$$T_n(E-W) = \sum_m E_{nm} G_{nm}^2 \tag{15}$$

where the sum is over all the gravity coefficients of degree n, G_{nm} is the gravity coefficient, $N_{nm} = n(n+1) - (2n+1)m/2$, and $E_{nm} = (2n+1)m/2$. The ratio of the two sums (N-S to E-W) is shown in Fig. 14 for the gravity field Ceres18c and the gravity derived from constant density shape, where for both the larger hydrostatic coefficients J_2 and J_4 are excluded. For the low-degree gravity ($n = 2$–5) there is a E-W preference, but for higher degrees the gravity field is isotropic. For Vesta, there is a preference for greater N-S variations (Bills et al., 2014) than those of Ceres.

6. Rotational and landmark results for Ceres

The Ceres gravity field is given in a body-fixed frame defined by an IAU right ascension α, declination δ, and prime meridian ($W_0 + \dot{W}d$, where d is in days past the J2000 epoch) coordinate system relative to the inertial ICRF (Archinal et al., 2011).

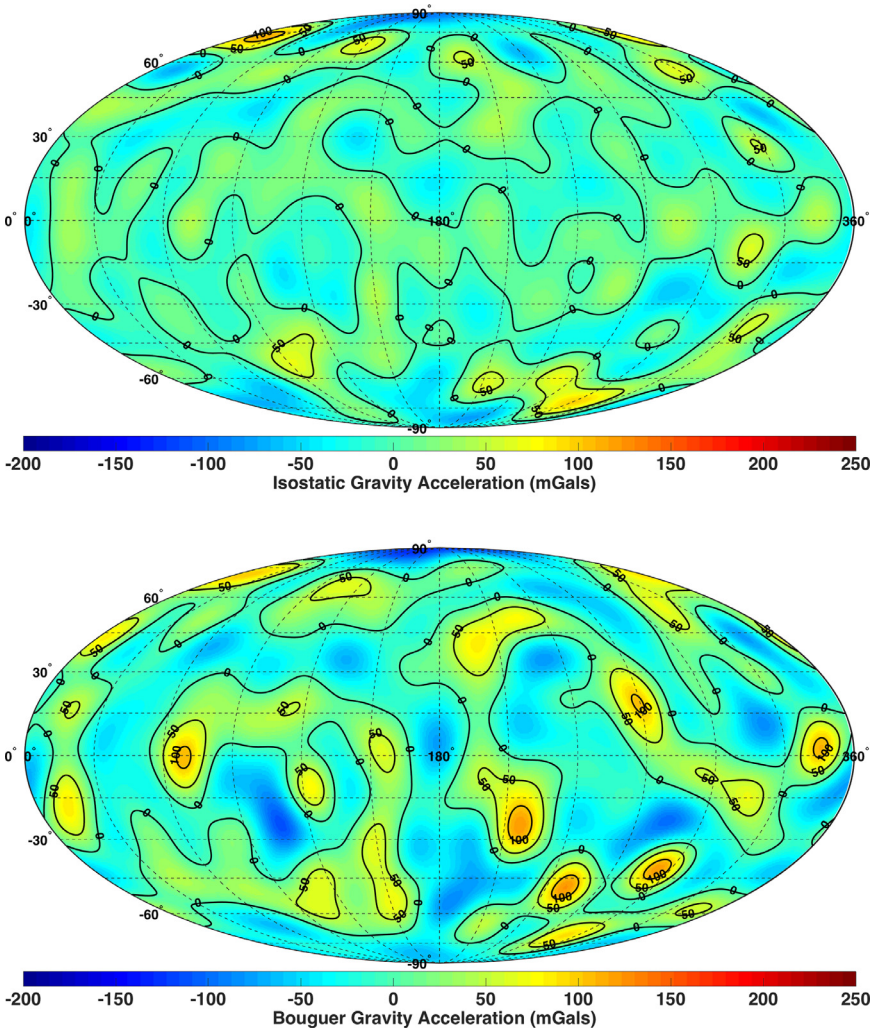

Fig. 13. Isostatic (top) and Bouguer (bottom) gravity anomaly maps for harmonic degrees $n = 5$–14. The anomalies are radial gravity mapped to a 482.0 × 445.9-km ellipsoid. The first map assumes Airy isostatic compensation and the Bouguer anomaly (gravity minus gravity from topography) map is determined by topography with a constant crustal density. Both maps assume a crustal density of 1400 kg/m^3. The same scale is used as Fig. 7 to show how well the anomalies are removed. Contour lines are displayed at intervals of 50 mGals.

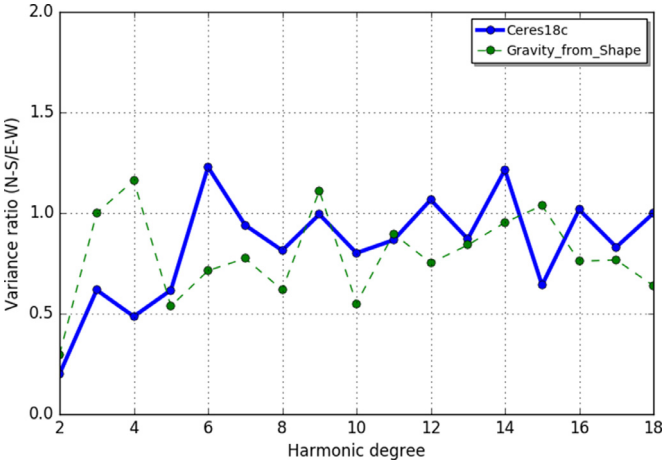

Fig. 14. The isotropic ratio of the north-south slope variance to that in the east-west direction for the gravity field of Ceres (Ceres18c) and the gravity field derived from the shape of Ceres. The gravity field of Ceres shows higher amplitudes in the east-west direction for the low-degree harmonics but is isotropic for the higher-degrees ($n > 5$).

Prior to Dawn, the pole location uncertainty for Ceres was near 5° from Hubble images (Thomas et al., 2005) and the rotation rate was well determined from many years of light curve data $\dot{W} = 952.1532 \pm 0.0002$ deg/day (Chamberlain et al., 2007). The initial Ceres gravity results from HAMO improved the pole location uncertainties by about a factor of 1000 (Park et al., 2016), and achieved uncertainties in the rotation rate that are comparable to the light curve analysis. With the addition of LAMO data, the pole location is improved by another factor of 10, and the rotation rate improves upon the light-curve analysis by a factor of ~100.

The results for Ceres' orientation are given in Table 4 and include the separate contributions from the DSN and optical landmark data in terms of uncertainties. Based upon comparisons between independent solutions with MIRAGE and Monte, the more realistic given uncertainties are the formal uncertainties increased by a factor of six for the pole location and three for the rotation rate. The reason for the different scaling factor is that the pole location is generally determined by the DSN data and requires a larger scale due to the attitude maneuvers and red-noise solar plasma contributions to the Doppler. The spin rate, however, is mostly determined by the optical data. The estimate for W_0 is obtained by fixing the y-position of the Kait landmark to zero in the global solution for gravity, orientation and landmark locations.

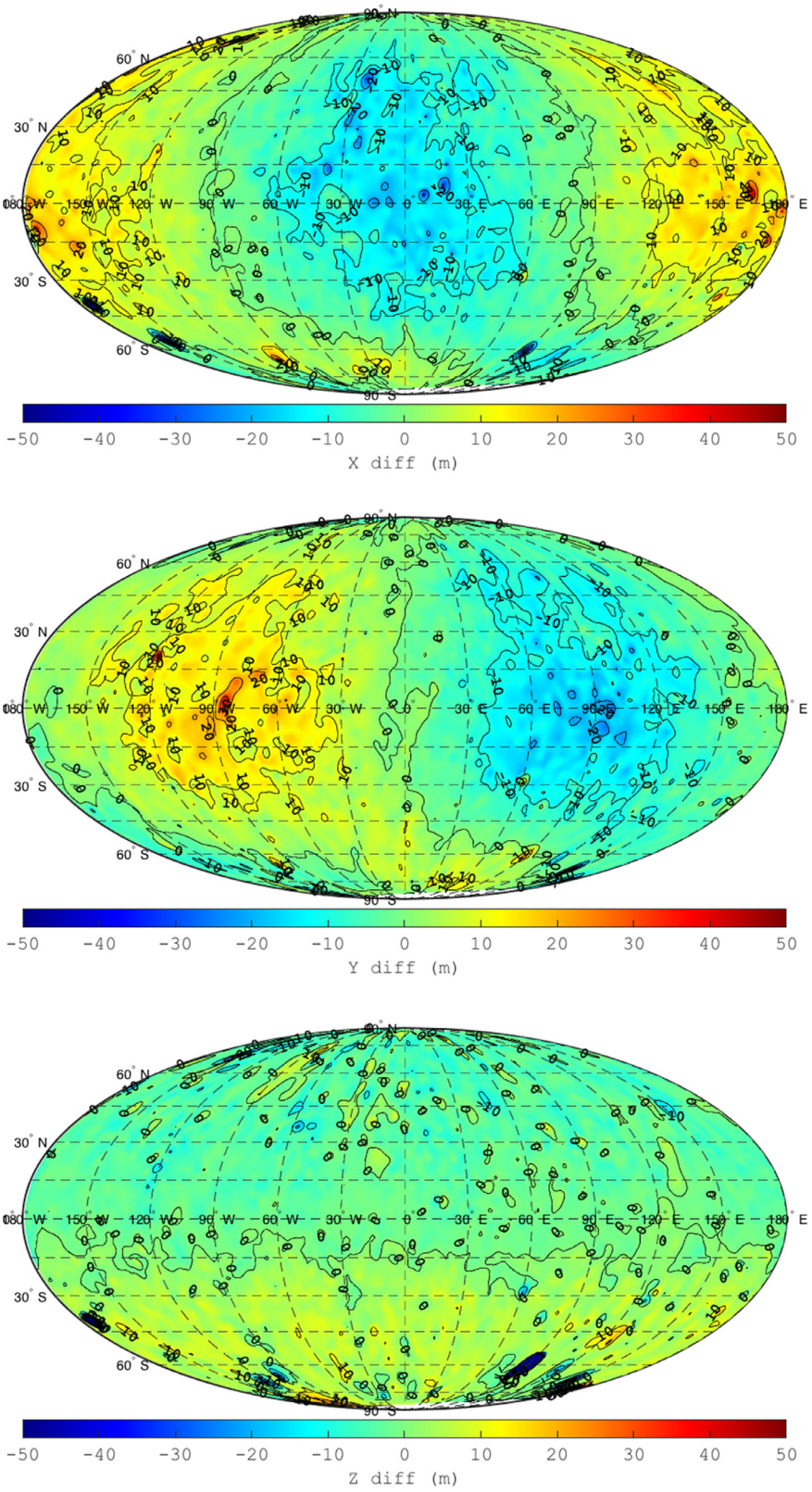

Fig. 15. Differences in the landmark solutions between the LAMO shape model from SPC and landmarks from the global gravity solution. The differences are for the X (top), Y (middle), and Z (bottom) coordinates.

Table 4
Ceres orientation solutions. Given uncertainties represent realistic errors where the formal sigmas are increased by 6× for the pole location and 3× for the rotation rate. The pole location is mostly determined by the contributions of the DSN data whereas the prime meridian and spin rate are mostly determined by the optical data.

Solution	α (deg)	δ (deg)	W_0 (deg)	dW/dt (deg/day)
Thomas et al. (2005) Chamberlain et al. (2007) (pre-Dawn)	291.± 5.	59 ± 5	170.9	952.1532 ± 0.0002
Park et al. (2016) (Dawn HAMO)	291.421 ± 0.007	66.758 ± 0.002	170.65	N/A
This paper (Dawn HAMO+LAMO)	291.42744 ± 0.00022	66.76065 ± 0.00022	170.311 ± 0.012	952.153264 ± 0.000002
DSN data only uncertainties	±0.00052	±0.00025		±0.000030
Optical data only uncertainties	±0.00320	±0.00240		±0.000006

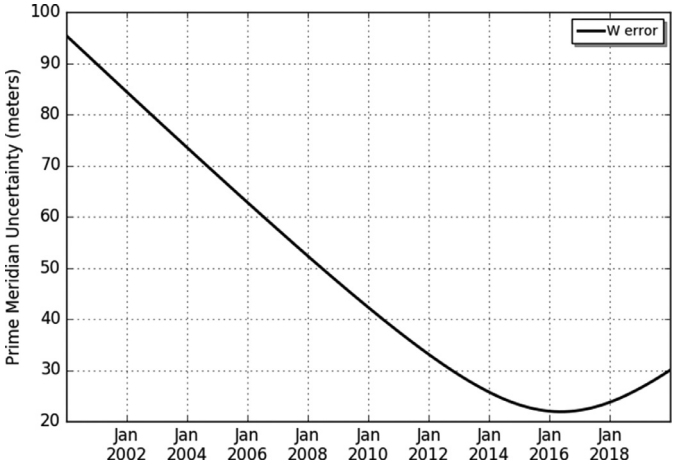

Fig. 16. The uncertainty in the location of the prime meridian in the ICRF system from the J2000 epoch. The minimum error occurs during the time Dawn is at Ceres. The errors displayed include a factor of 3 times the formal error to give more realistic errors.

This forces the prime meridian to pass through the Kait crater. All other landmark positions are estimated with a large *a priori* uncertainty of 3-km from the *a priori* value obtained from the shape modeling using SPC.

Comparisons of MIRAGE and Monte solutions with similar but not identical modeling have also been used to indicate orbit uncertainties and landmark position errors. For the LAMO orbit, differences indicate an accuracy of typically one meter in the radial direction and about 10-meters in the other along-track and orbit normal directions, as expected from the pixel size of the landmark observations. As with the Vesta results (Konopliv et al., 2014), we also looked at the differences in the landmark solutions between MIRAGE (or Monte) and the landmarks solutions from the shape modeling SPC software. The landmark position solutions are within the formal uncertainties of the MIRAGE landmark estimates and are typically 20 m. The landmark differences are shown in Fig. 15, and are less than the errors experienced for the Vesta studies (Konopliv et al., 2014), especially for the Z-component (80-m vs. 10-m). The agreement of the Ceres landmark solutions is even more apparent due to the larger pixel size on the surface of Ceres (35-m) than that of Vesta (16-m).

The prime meridian location uncertainty is primarily given by the uncertainty in the landmark position of the Kait crater. As mentioned above, the landmark position estimates, like those surrounding the Kait crater, have a typical uncertainty of 10–30 m in position. The uncertainty in the prime meridian location angle W in terms of W_0 and $\dot{W}$ uncertainties is given by

$$\sigma_W^2 = \sigma_{W_0}^2 + 2t\rho\sigma_{W_0}\sigma_{\dot{W}} + t^2\sigma_{\dot{W}}^2, \quad (16)$$

where t is the time past the J2000 epoch and ρ is the error correlation between W_0 and $\dot{W}$, which is −0.97 in our case. Fig. 16 displays the uncertainty in the prime meridian versus time past J2000. The uncertainty at the time of the Dawn data collection is a minimum of 22 m.

7. Ceres ephemeris solution

The global Ceres gravity solution includes estimates of the gravity, rotation parameters, landmark positions and the ephemeris or heliocentric orbit of Ceres. In the global solution, the Ceres ephemeris solution is a linear correction in set III elements (Brouwer and Clemence, 1961) to the pre-Dawn Ceres ephemeris solution from historical Earth-based images. The ephemeris is then iterated for every global solution until set III corrections are negligible. After the determination of the final Ceres gravity solution Ceres18c, a second approach was used to generate a new Ceres ephemeris solution using JPL's small body ephemeris software (Yeomans et al., 1992). In this method, the Earth based images from 1830 to the current date were merged with 1.5 years of Dawn ranging data from Feb. 2015 to Sept. 2016.

The range data to the Dawn spacecraft from multiple DSN stations are shifted from the spacecraft position to the center-of-mass of Ceres by resolving the round trip light equation (Moyer et al., 2000). The range observation is then equivalent to a radar bounce observation to the center of Ceres. The two main error sources in the observation are any errors in the spacecraft orbit and delay in the range measurement due to solar plasma. The accuracy of the range measurement (including spacecraft orbit errors) is near 4 m for the entire Dawn mission duration, which is slightly larger than the raw range measurement accuracy from the DSN of about one meter. This method of ephemeris improvement is the same technique that was applied to the Vesta ephemeris improvement by Dawn (Konopliv et al., 2014) and the Mars ephemeris solution (Konopliv et al., 2011b). Similar methods also were used to improve the orbit of near-Earth asteroid 433 Eros from NEAR spacecraft range data (Konopliv et al., 2002).

The initial Ceres ephemeris accuracy from historical pre-Dawn data is near 40 km at the time of encounter for Dawn at Ceres. Ceres orbit errors within the years 1850–2150 are 15 km, between 35–140 km and 30-km for the heliocentric radial, cross-track and along-track uncertainties, respectively. With the addition of 17 months of Dawn range data (∼4 m) at Ceres, the ephemeris uncertainty significantly improves by more than two orders of magnitude for the 300-year time span displayed (Fig. 17), and with the error at the Dawn time at Ceres being near 10 m. The maximum error in the Ceres' ephemeris propagated about 150 years into the future is an along-track error of less than 1 km. The results for the post-Dawn Ceres ephemeris solution are noticeably better (∼10–100×) than the results for Vesta (Konopliv et al., 2014) due to the improved accuracy of the range data (4-m vs 15-m) and the extended time at Ceres (18 months vs. 9 months).

Residuals in the historical optical and Dawn range data used in the orbit fit are shown in Figs. 18 and 19, respectively. The available optical astrometry spans the years 1830–2014 (6929 measurements) and converted Dawn spacecraft range data (294 X-band measurements from February 2015 to September 2016 representing one Dawn range observation per available DSN pass). Optical data were weighted appropriately based on a model described by Chesley et al. (2010), with weights ranging from about 3 to 0.2″. Recent optical data were further improved by taking into account

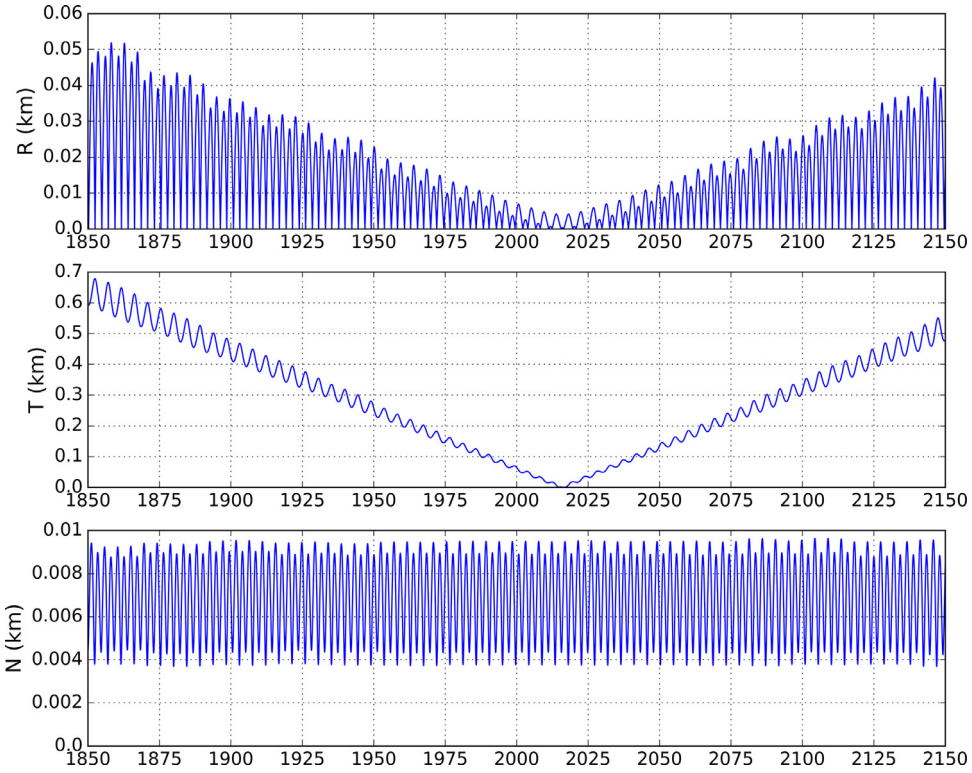

Fig. 17. The Ceres heliocentric ephemeris uncertainty (Radial R, along-track T, normal to the orbit plane N) with range data from the Dawn mission. The solution uncertainty is based upon Earth based images of Ceres from 1830 to present and Dawn range data from Feb. 2015 to Sept. 2016.

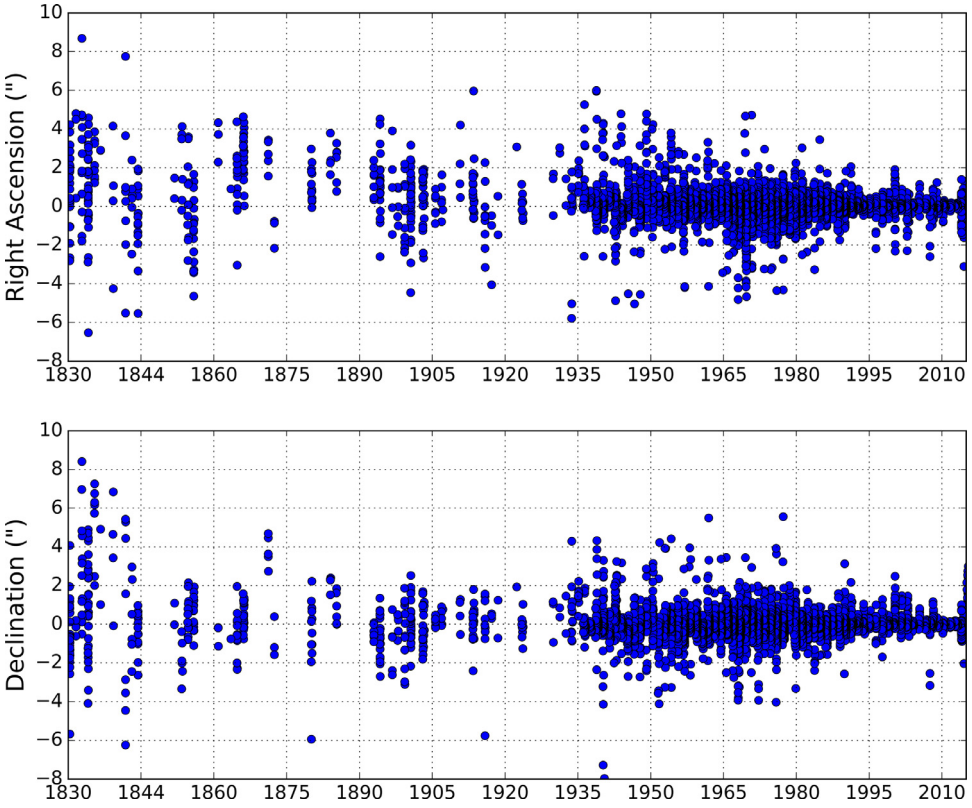

Fig. 18. Post-fit residuals of the Earth-based image data of Ceres used in the ephemeris solution.

Table 5
Ceres heliocentric ecliptic J2000 osculating orbital elements and associated formal uncertainties at epoch 2016-Jan-01.

Element	Prior Solution Value	New Solution Value	Prior Solution Uncertainty 1-sigma	New Solution Uncertainty 1-sigma	Uncertainty Ratio
e	0.0757568473703635	0.0757567879470938	3.07×10^{-8}	5.59×10^{-12}	5490
q (AU)	2.5584024869774460	2.5584026360483080	8.47×10^{-8}	2.70×10^{-11}	3135
T (JD)	2,456,552.9240285019	2,456,552.9240954894	1.15×10^{-4}	6.20×10^{-9}	18,523
Ω (deg)	80.32229952274804	80.32230171268262	1.99×10^{-5}	5.66×10^{-9}	3520
ω (deg)	72.72693645731393	72.72695694436509	3.11×10^{-5}	5.47×10^{-9}	5683
i (deg)	10.59169090811561	10.59168890415670	3.80×10^{-6}	9.30×10^{-10}	4089
a (AU)	2.768105427341641	2.768105410658789	2.97×10^{-9}	1.25×10^{-11}	237
P (days)	1682.179620146136	1682.179604938865	2.71×10^{-6}	1.14×10^{-8}	237
M (deg)	178.81999409384740	178.81998137454040	2.47×10^{-5}	4.62×10^{-10}	53,417

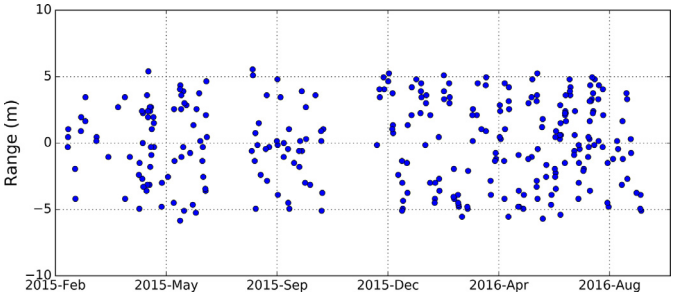

Fig. 19. Post-fit residuals of the Dawn range data mapped to the Ceres center-of-mass used in the ephemeris solution.

known star catalog biases (Chesley et al., 2010). Dawn range data were weighted at 4 m for two-way range (or 2 m in each direction), a level consistent with post-fit residuals and uncertainties in the Dawn spacecraft orbit relative to Ceres. The dynamical model used in the JPL asteroid orbit determination code considers perturbations from all the planets, the moon, and Pluto from JPL's planetary ephemeris DE-431 (Folkner, 2014) and the 15 most massive asteroids (excluding Ceres): 2 Pallas, 4 Vesta, 10 Hygiea, 3 Juno, 6 Hebe, 7 Iris, 15 Eunomia, 16 Psyche, 29 Amphitrite, 52 Europa, 65 Cybele, 87 Sylvia, 88 Thisbe, 511 Davida, and 704 Interamnia. The model also includes the effects of general relativity and solar corona effects on the X-band range data.

Although the orbit of Ceres prior to the Dawn encounter was well established, use of Dawn range data has substantially improved the orbit, reducing the uncertainties by at least two orders of magnitude for all orbital elements. The best-fit solution before and after Dawn that was obtained using osculating orbital elements with an epoch during the Dawn time at Ceres is shown in Table 5 with the corresponding formal uncertainties. The formal uncertainties are optimistic since only a limited number of asteroids are used in computing perturbations to the Ceres orbit.

Acknowledgments

We thank Bill Owen for help with the optical software, the Dawn Navigation team (Nick Mastrodemos, Don Han, and Brian Kennedy) for discussion and modeling information, and Alan Chamberlin for discussions on the Ceres and Vesta ephemeris. The research described in this paper was carried out at the Jet Propulsion Laboratory, California Institute of Technology, under contract with the National Aeronautics and Space Administration.

References

Archinal, B.A., et al., 2011. Report of the IAU working group on cartographic coordinates and rotational elements. 2009. Celes. Mech. Dyn. Astron. 109, 101–135.

Asmar, S.W., Armstrong, J.W., Iess, L., Tortora, P., 2005. Spacecraft Doppler tracking: noise budget and achievable accuracy in precision radio science observations. Radio Sci. 40, RS2001. doi:10.1029/2004RS003101.

Baer, J., Chesley, S.R., Matson, R.D., 2011. Astrometric masses of 26 asteroids and observations on asteroid porosity. Astron. J. 141 (5). doi:10.1088/0004-6256/141/5/143.

Bierman, G.J., 1977. Factorization Methods for Discrete Sequential Estimation. Academic Press, New York, p. 241.

Bills, B.G., Asmar, S.W., Konopliv, A.S., Park, R.S., Raymond, C.A., 2014. Harmonic and statistical analyses of the gravity and topography of Vesta. Icarus 240, 161–173. http://dx.doi.org/10.1016/j.icarus.2014.05.033.

Bills, B.G., Lemoine, F.G., 1995. Gravitational and topographic isotropy of the Earth, Moon, Mars, and Venus. J. Geophys. Res. 100 (E12) 26,275-26,295.

Brouwer, D., Clemence, G., 1961. Methods of Celestial Mechanics. Academic Press, New York.

Chamberlain, M.A., Sykes, M.V., Esquerdo, G.A., 2007. Ceres lightcurve analysis – period determination. Icarus 188, 451–456. doi:10.1016/j.icarus.2006.11.025.

Chesley, S.R., Baer, J., Monet, D.G., 2010. Treatment of star catalog biases in asteroid astrometric observations. Icarus 210, 158–181.

Ermakov, A.I., Fu, R.R., Castillo-Rogez, J.C., Raymond, C.A., Park, R.S., Preusker, F., Russell, C.T., Smith, D.E., Zuber, M.T., 2017. Constraints on Ceres' internal structure and evolution from its shape and gravity measured by the Dawn spacecraft. Submitted to. J. Geophys. Res.

Fienga, A., Laskar, J., Morley, T., Manche, H., Kuchynka, P., Le Poncin-Lafitte, C., Budnik, F., Gastineau, M., Somenzi, L., 2009. INPOP08, a 4-D planetary ephemeris: from asteroid and time-scale computations to ESA Mars Express and Venus Express contributions. Astron. Astrophys. 507 (3), 1675–1686. doi:10.1051/0004-6361/200911755.

Folkner, W.M., Charlot, P., Finger, M.H., Williams, J.G., Sovers, O.J., Newhall, X.X., Standish, E.M., 1994. Determination of the extragalactic-planetary frame tie from joint analysis of radio interferometric and lunar laser ranging measurements. Astron. Astrophys. 287, 279–289.

Folkner, W.M., Williams, J.G., Boggs, D.H., Park, R.S., Kuchynka, P., 2014. The planetary and lunar ephemeris DE 430 and DE 431. The Interplanetary Network Progress Rep. 42-196. Pasadena, CA: Jet Propulsion Laboratory.

Fu, R., Ermakov, A.I., Marchi, S., Castillo-Rogez, J.C., Raymond, C.A., Hager, B.H., Zuber, M.T., King, S.D., Bland, M.T., De Sanctis, M.C., Preusker, F., Russell, C.T., 2017. The interior structure of Ceres as revealed by surface topography. Submitted to. Earth Planet. Sci. Lett.

Grafarend, E., Engels, J., 1994. The convergent series expansion of the gravity field of a starshaped body. Manuscripta Geodaeitica 19, 18–30.

Gaskell, R.W., Barnouin-Jha, O.S., Scheeres, D.J., Konopliv, A.S., Mukai, T., Abe, S., Saito, J., Ishiguro, M., Kubota, T., Hashimoto, T., Kawaguchi, J., Yoshikawa, M., Shirakawa, K., Kominato, T., Hirata, N., Demura, H., 2008. Characterizing and navigating small bodies with imaging data. Meteorit. Planet. Sci. 43, 1049–1061.

Hemingway, D.J., Matsuyama, I., 2017. Isostatic equilibrium in spherical coordinates and implications for crustal thickness on the Moon, Mars, Enceladus, and elsewhere. Geophys. Res. Lett. 44. doi:10.1002/2017/GL073334.

Heiskanen, W.A., Moritz, H., 1967. Physical Geodesy Freeman W.H., and Company, San Francisco and London.

Kaula, W.M., 1966. Theory of Satellite Geodesy. Blaisdell Waltham, MA.

Konopliv, A.S., Park, R.S., Folkner, W.M., 2016. An improved JPL Mars gravity field and orientation from Mars Orbiter and Lander tracking data. Icarus 274, 253–260.

Konopliv, A.S., Asmar, S.W., Park, R.S., Bills, B.G., Centinello, F., Chamberlin, A., Ermakov, A.I., Gaskell, R., Rambaux, N., Raymond, C.A., Russell, C.T., Smith, D.E., Tricarico, P., Zuber, M.T., 2014. The Vesta gravity field, spin pole and rotation period, landmark positions, and ephemeris from the Dawn tracking and optical data. Icarus 240, 103–117. doi:10.1016/j.icarus.2013.09.005.

Konopliv, A.S., Asmar, S.W., Bills, B.FG., Mastrodemos, N., Park, R.S., Raymond, C.A., Smith, D.E., Zuber, M.T., 2011a. The Dawn gravity investigation at Vesta and Ceres. Space Sci. Rev. 163, 461–486. doi:10.1007/s11214-011-9794-8.

Konopliv, A.S., Asmar, S.W., Folkner, W.M., Karatekin, O., Nunes, D.C., Smrekar, S.E., Yoder, C.F., Zuber, M.T., 2011b. Mars high resolution gravity fields from MRO, Mars seasonal gravity, and other dynamical parameters. Icarus 211, 401–428.

Konopliv, A.S., Yoder, C.F., Standish, E.M., Yuan, D.-N., Sjogren, W.L., 2006. A global solution for the Mars static and seasonal gravity, Mars orientation, Phobos and Deimos masses, and Mars ephemeris. Icarus 182, 23–50.

Konopliv, A.S., Miller, J.K., Owen, W.M., Yeomans, D.K., Giorgini, J.D., Garmier, R., Barriot, J.-P., 2002. A global solution for the gravity field, rotation, landmarks, and ephemeris of Eros. Icarus 160, 289–299.

Konopliv, A.S., Banerdt, W.B., Sjogren, W.L., 1999. Venus gravity: 180th degree and order model. Icarus 139, 3–18.
Krening, S.C., Semenov, B.V., Acton, C.H., 2012. DAWN SPICE KERNELS V1.0, DAWN-M/A-SPICE-6-V1.0. NASA Planet. Data Syst. https://pds.nasa.gov/ds-view/pds/viewProfile.jsp?dsid=DAWN-M/A-SPICE-6-V1.0.
Krogh, F.T., 1973. Changing stepsize in the integration of differential equations using modified divided differences, JPL Technical Memorandum No. 312, Section 914.
Kuchynka, P., Folkner, W.M., 2013. A new approach to determining asteroid masses from planetary range measurements. Icarus 222, 243–253. doi:10.1016/j.icarus.2012.11.003.
Lambeck, K., 1988. Geophysical Geodesy. Oxford University Press, ClarendonOxford, p. 718.
Lawson, C.L., Hanson, R.J., 1995. Solving least squares problems. SIAM Classics in Applied Mathematics, 15. Society for Industrial and Applied Mathematics, Philadelphia.
Michalak, G., 2000. Determination of asteroid masses - I. (1) Ceres, (2) Pallas, and (4) Vesta. Astron. Astrophys. 360, 363–374.
Moyer, T.D., 2000. Formulation for observed and computed values of deep space network data types for navigation, monograph 2 of deep space communications and navigation series. JPL Publication 00-7. Jet Propulsion Laboratory, California Institute of Technology, Pasadena, CA.
Moyer, T.D., 1971. Mathematical Formulation of the Double-Precision Orbit Determination Program (DPODP). Jet Propulsion Laboratory, California Institute of Technology, Pasadena, CA JPL Technical Report 32-1527.
Owen, Jr.,W.M., Wang, T.C., Harch, A., Bell, M., Peterson, C., 2001. NEAR optical navigation at Eros. AAS Paper 01-376, Presented at AAS/AIAA Astrodynamics Specialists Conference Quebec City, Quebec, Canada.
Park, R.S., et al., 2017. High-resolution topography of Ceres from Dawn imaging data. to be submitted.
Park, R.S., Konopliv, A.S., Bills, B.G., Vaughan, A.T., Rambaux, N., Castillo-Rogez, J.C., Raymond, C.A., Russell, C.T., Toplis, M.J., Ermakov, A., Zuber, M.T., 2016. A partially differentiated interior for (1) Ceres deduced from its gravity field and shape. Nature 537, 515–517. doi:10.1038/nature18955.
Park, R.S., Konopliv, A.S., Asmar, S.W., Bills, B.G., Gaskell, R., Raymond, C.A., Smith, D.E., Toplis, M.J., Zuber, M.T., 2014. Gravity field expansion in ellipsoidal harmonic and polyhedral internal representations applied to Vesta. Icarus 240, 118–132. doi:10.1016/j.icarus.2013.12.005.
Pitjeva, E.V., 2005. High-precision ephemerides of planets - EPM and determination of some astronomical constants. Solar Syst. Res. 39, 176–186.
Rambaux, N., Chambat, F., Castillo-Rogez, J.C., 2016. Third-order development of shape, gravity and moment of inertia for highly flattened celestial bodies – application to Ceres. Astron. Astrophys. 584 (A127). doi:10.1051/0004-6361/201527005.
Rambaux, N., Castillo-Rogez, J., Dehant, V., Kuchynka, P., 2011. Constraining Ceres' interior from its rotational motion. Astron. Astrophys. 535 (A43). doi:10.1051/0004-6361/201116563.
Schubert, G., Anderson, J.D., Spohn, T., McKinnon, W.B., 2004. Interior composition, structure and dynamics of the Galilean satellites. In: Bagenal, Fran, E, Timothy, William, Dowling, McKinnon, B. (Eds.), Jupiter. The Planet, Satellites and Magnetosphere. In: Cambridge Planetary Science, 1. Cambridge University Press, pp. 281–306. ISBN 0-521-81808-7.
Standish, E.M., 2001. Suggested GM values for Ceres, Pallas, and Vesta. JPL Interoffice Memorandum, 312.F-01-006, April 11, 2001.
Tapley, B.D., Schutz, B.E., Born, G.H., 2004. Statistical Orbit Determination. Elsevier, Boston, p. 547.
Thomas, P.C., Parker, J. Wm. McFadden, L.A., Russell, C.T., Stern, S.A., Sykes, M.V., Young, E.F., 2005. Nature 437, 224–226, doi:10.1038/nature03938.
Thomas, V.C., Makowski, J.M., Brown, G.M., McCarthy, J.F., Bruno, D., Cardoso, J.C., Chiville, W.M., Meyer, T.F., Nelson, K.E., Pavri, B.E., Termohlen, D.A., Violet, M.D., Williams, J.B., 2011. The Dawn spacecraft. Space Sci. Rev. 163, 175–249. doi:10.1007/s11214-011-9852-2.
Turcotte, D.L., McAdoo, D.C., 1979. Geoid anomalies and the thickness of the lithosphere. J. Geophys. Res. 84, 2381–2387.
Wieczorek, M.A., Phillips, R.J., 1998. Potential anomalies on a sphere: applications to the thickness of the lunar crust. J. Geophys. Res. 103 (E1), 1715–1724.
Williams, J.G., et al., 2014. Lunar interior properties from the GRAIL mission. J. Geophys. Res. Planets 119, 1546–1578. doi:10.1002/2013JE004559.
Yeomans, D.K., Chodas, P.W., Keesey, M.S., Ostro, S.J., Chandler, J.F., Shapiro, I.I., 1992. Asteroid and comet orbits using radar data. Astron. J. 103, 303–317.
Yoder, C.F., 1995. Astrometric and geodetic properties of Earth and the Solar System. In: Ahrens, T.J. (Ed.), Global Earth Physics. American Geophysical Union. doi:10.1029/RF001p0001.